LamaH-CE | *La*rge-Sa*m*ple D*a*ta for *H*ydrology and Environmental Sciences for Central Europe

Christoph Klingler, Karsten Schulz, Mathew Herrnegger

Institute for Hydrology and Water Management, University of Natural Resources and Life Sciences, Vienna, 1190, Austria

5   *Correspondence to*: Christoph Klingler (christoph.klingler@boku.ac.at)

Abstract. Very large and comprehensive datasets are increasingly used in the field of hydrology. Large-sample studies provide insights into the hydrological cycle that might not be available with small-scale studies. LamaH (*La*rge-Sa*m*ple D*a*ta for *H*ydrology) is a new dataset for large-sample studies and comparative hydrology in Central Europe. It covers the entire upper Danube to the state border Austria / Slovakia, as well as all other Austrian catchments including their foreign upstream areas.

10   LamaH covers an area of about 170 000 km² in 9 countries, ranging from lowland regions characterized by a continental climate to high alpine zones dominated by snow and ice. Consequently, a wide diversity of properties is present in the individual catchments. We represent this variability in 859 gauged catchments with over 60 catchment attributes, covering topography, climatology, hydrology, land cover, vegetation, soil and geological properties. LamaH further contains a collection of runoff time series as well as meteorological time series. These time series are provided with daily and hourly resolution. All

15   meteorological and the majority of runoff time series cover a span of over 35 years, which enables long-term analyses with a high temporal resolution. The runoff time series are classified by over 20 attributes including information about human impacts and indicators for data quality and completeness. The structure of LamaH is based on the well-known CAMELS datasets. In contrast, however, LamaH does not only consider independent basins, covering the full upstream area. Intermediate catchments are covered as well, which allows together with novel attributes to consider the hydrological network and river topology in

20   applications. We describe not only the used basic datasets and methodology of data preparation, but also focus on possible limitations and uncertainties. LamaH contains additionally results of a conceptual hydrological baseline model for checking plausibility of the inputs as well as benchmarking. Potential applications of LamaH are outlined as well, since it is intended to serve as a uniform data basis for further research. LamaH is available at https://doi.org/10.5281/zenodo.4525244 (Klingler et al., 2021).

25   **1 Introduction**

Hydrology and hydrological processes are characterized by high spatiotemporal variability. Runoff generation in small-scale, alpine catchments with steep and complex topography is dominated by different processes compared to lowland rivers with flat topography. The water balance in an energy-limited, humid catchment in Europe is completely different than, for example, in a water-limited catchment in dry (semi-) arid regions in Africa or Australia. A water droplet flowing via the Russian Lena

30 river into the Arctic Sea has a completely different biography than a water droplet from Rwanda in Central Africa, which reaches the Mediterranean Sea via the Nile after more than 6 600 km. Boundary conditions and major drivers for the differences are the catchment attributes, which can be described by characteristics regarding topography, hydro-climate, land cover, geology and soil conditions.

In order to deepen our understanding of the hydrological process and further increase the reliability of (hydrological) models,

35 it is necessary to account for this spatiotemporal variability in our approaches. A number of international initiatives (e.g. Distributed Model Intercomparison Project (DMIP; Smith et al., 2004); Inter-Sectoral Impact Model Intercomparison Project (ISI-MIP; Warszawski et al., 2014); Model Parameter Estimation Project (MOPEX; Duan et al., 2006) or Hydrological Ensemble Prediction Experiment (HEPEX; Schaake et al., 2007)) have been launched in recent decades with the aim to advance the prediction of hydrologic variables through comprehensive model benchmarking in different regions of the world.

40 New efforts strive for creating homogeneous and consistent datasets, which serve as a solid basis towards the development of new modelling approaches.

In this context, a trend towards more complete and extensive datasets is apparent: 1) Remote sensing has enabled consistent and global mapping of Earth's atmosphere and surface. 2) New software platforms or applications for obtaining and processing these mostly very data-intense (e.g. regarding data volumes) remote sensing products facilitate their applicability. Examples

45 of such platforms are "Google Earth Engine" (GEEa, 2021; GEEb, 2021; Gorelik et al., 2017; Klingler et al., 2020), the "Copernicus Open Access Hub" (COPa, 2021) or the "Copernicus Climate Data Store" (COPb, 2021). 3) There is growing awareness that our understanding of the complex hydrological processes can be deepened through "large-sample" studies (Gupta et al., 2014). Large-sample hydrology (LSH) includes information from a broad range of different watersheds in order to derive robust conclusions (Addor et al., 2019). Several research groups in different areas of hydrology have already focused

50 on LSH for this reason (e.g. Berghuijs et al., 2014; Blöschl et al., 2019a; Döll et al., 2016; Gudmundsson et al., 2019; Luke et al., 2017; Kuentz et al., 2017; Singh et al., 2014; Van Lanen et al., 2013). 4) Finally, data-driven models and deep learning approaches have recently gained significant attention in hydrology (Sit et al., 2020). Independent from the fact that these developments are controversially discussed (Nearing et al., 2020), their excellent performance in time series prediction, including in an ungauged setting (e.g. Kratzert et al., 2019a), is related to the ability of machine learning to identify patterns

55 and relationships in data (Kratzert et al., 2019b). These approaches however strongly depend on the availability of large-sample datasets (e.g. Kratzert et al., 2019a; 2019b; Kratzert et al., 2018).

Given the workload and scope of large-sample studies, it is reasonable to differentiate between dataset preparation and the subsequent investigation (i.e. publish the findings separately), which allows a more detailed description of the dataset and enables easier access. A selection of previously published "large-sample" datasets can be found in Table 1 in Gupta et al.

60 (2014). Other datasets for large-sample hydrologic applications include the Global Runoff Reconstruction (Ghiggi et al., 2019), Global Streamflow Indices and Metadata Archive (Do et al., 2018; Gudmundsson et al., 2018), HydroATLAS (Linke et al., 2019), HydroSHEDS (Lehner et al., 2008), and the CAMELS (CAtchment Attributes and MEteorology for Large-sample Studies; Addor et at., 2017a; and references in the following section) collection. The CAMELS datasets are characterized by

a consistent data preparation and consistent structure. Furthermore, potential limitations as well as uncertainties are discussed

65 there in detail. However, CAMELS only include data for independent catchments, covering the full upstream area, and not for an interconnected river network (Addor et al., 2019). The first CAMELS dataset was published by Addor et al. (2017a) and Newman et al. (2015) for the contiguous territory of the United States, containing data for 671 watersheds. Further CAMELS datasets for Chile (Alvarez-Garreton et al., 2018; 516 catchments), Brazil (Chagas et al., 2020; 897 catchments), and Great Britain (Coxon et al., 2020; 671 catchments) followed later. CAMELS datasets always represent a composite of

70 hydrometeorological time series and static catchment attributes aggregated to polygons, which cover the full upstream area. The question, how reasonable and applicable meteorological and catchment attributes are, when aggregated to the full upstream area, is critical, especially for large basins.

LamaH (*La*rge-*Sa*mple *Da*ta for *H*ydrology) is a new dataset for LSH (859 gauged catchments) in Central Europe and is generally based on the structure of the CAMELS datasets. LamaH therefore includes runoff time series, meteorological

75 forcings as well as static catchment attributes, but offers a few novelties. For example, LamaH includes a basin delineation that represents the inter-catchment area (difference area or intermediate catchments) of neighboring gauges, in addition to the usual basin delineation used in CAMELS datasets, which is equivalent to the topographic (delineated only considering terrain features and ignoring potential subsurface cross-basin flows) catchment area of the individual gauges. Supplementary attributes such as the gauge topology, as well as the flow length and gradient between two adjacent gauges, are added to specify the

80 interconnected hydrologic network. This enables, for example, to model the local runoff generation in the intermediate catchments and the river routing separately. A further novelty of LamaH is the finer resolution of the provided hydrometeorological time series (daily and hourly). Time series with hourly resolution are crucial for a reliable result when modelling, for instance, the river routing or snow or glacier driven processes, where the observed signal in runoff shows a distinct diurnal pattern.

85 This paper is organized as follows: After a description of the project area (section 2) and included basins and catchments (section 3), the preparation of the hydrometeorological time series are described in section 4. Section 5 is about static catchment attributes and shows their spatial distribution. The set-up as well as the results of a hydrological baseline model are described in section 6. Additionally, uncertainties, limitations and restrictions of the used data sources or model outputs are discussed. Finally, section 7 includes a summary and an outlook of possible applications of LamaH.

90 **2 Domain of coverage**

LamaH covers an area of about 170 000 km² in 9 countries in Central Europe (Austria, Germany, Czech Republic, Switzerland, Slovakia, Italy, Liechtenstein, Slovenia and Hungary; sorted by descending contributing area). Its scope includes the upper Danube to the Austrian / Slovakian border, as well as all other catchment areas in Austria, including their adjacent upstream areas in neighboring countries. The Piz Bernina with 4 049 m a.s.l. represents the highest point within the project area, while

95 the lowest point at about 130 m a.s.l. is located at the most downstream gauge of the Austrian Danube. The dominant river is

the Danube (ICPDR, 2020; Prohaska et al., 2020), which has its source in the far west of the project area near Donaueschingen (Fig. 1, 8.2°E / 48.1°N). The catchments of Danube's main tributaries serve to divide the project area into 18 river regions (Table B1). An overview of the domain covered in LamaH with the river regions and the runoff gauges with their elevations is illustrated in Fig. 1. All river regions in the project except regions 1 and 11 are part of the Danube´s catchment. Water from regions declared with "Danube B" in Fig. 1 joins the Danube outside the project area in Hungary or Croatia. River region 1 covers the upper catchment of the Rhine from its sources to Lake Constance ("Rhine") and region 11 covers the Austrian catchment area of the Vltava, which is the largest tributary of the Elbe ("Elbe").
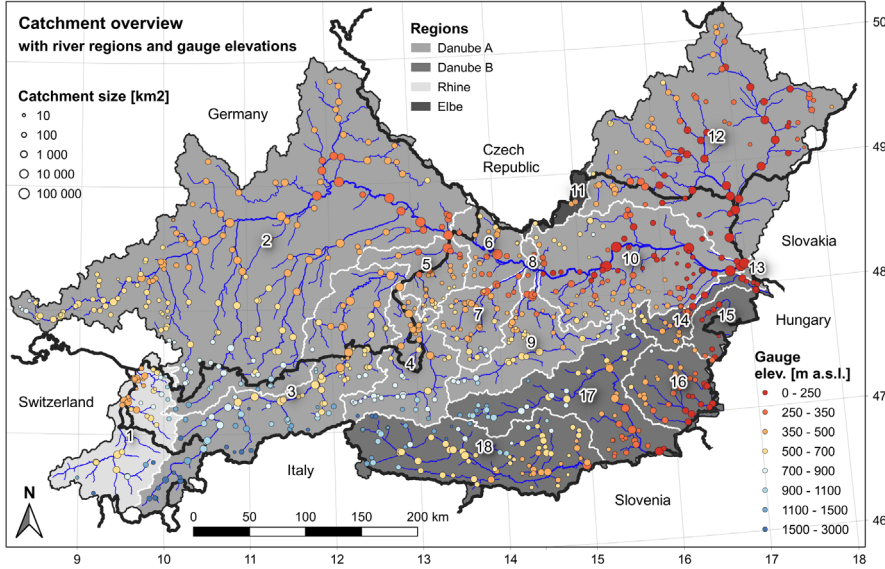
Fig. 1: Overview of the area covered in LamaH (grey tones), and the runoff gauges with gauge elevation (circle color) and catchment area (circle size). LamaH is divided into different river regions, which are bordered by the white lines. The black numbers are abbreviations for the individual regions, which are indicated in Table B1. The national borders are shown as thick black lines. Source of stream network: HydroATLAS (Linke et al., 2019). © EuroGeographics for the administrative boundaries.

3 Basin delineations and aggregation approaches

Most meteorological time series and catchment attributes included in LamaH are based on global datasets, which were provided either in raster or vector form. In LamaH, a catchment property or time step of a meteorological time series usually represents the mean computed across the topographic catchment of a gauge. Starting point for creating the aggregation polygons (catchments) were sub-basins from the datasets Digital Hydrological Atlas of Austria (HAO, 2007; full expansion) and HydroATLAS (Linke et al., 2019; level 12), which was used for areas not covered by HAO. The sub-basin outlets of HAO agree with the gauge locations. In contrast, the catchment boundaries of HydroATLAS were partially manually adjusted to guarantee that the basin outlets of the polygons agree with the gauging station locations. Since the sub-basin delineation in HAO and HydroATLAS were aggregated to represent the complete topographic catchment area upstream of a gauge, the different resolutions in the data sets did not matter. We refer to this method of basin delineation in the further text and the

dataset as "basin delineation A" (Fig. 2a). Plausibility of this type of basin delineation was checked by calculating the ratio between the area of the aggregated basins and the officially, e.g. in the metadata of the gauges, declared catchment area

120 ("area_ratio" in Table A1). The range of "area_ratio" lies between 0.89 and 1.34, with a standard deviation of 0.026. Catchments with larger deviation in area were manually checked and corrected if there was an obvious error. The median basin size over all 859 catchments of LamaH applying basin delineation A is 178 km², with a range of 4 to 131 247 km². Basin delineation A is identical to the delineation used in the CAMELS datasets. The advantage of basin delineation A is the independency between the basins, since the aggregation area fully represents the topographic catchment area of a gauge.

125 However, for gauges with larger catchments, aggregation with basin delineation A leads to a significant loss of information, as variability as well as small-scale characteristics are lost.

Therefore, basin delineation A is supplemented by a form of delineation (basin delineation B, 859 catchments) where the topographic catchment area of the next upstream gauge (may be none, one, or more) is subtracted from that of the current gauge (Fig. 2b). This results in the representation of intermediate catchments, which become part of a large connected river

130 network. The dependency among these intermediate catchments requires a catchment or gauge hierarchy (Fig. 2b, "HIERARCHY" in Table A1), as well as information regarding the upstream-downstream relationship ("NEXTUPID" or "NEXTDOWNID" in Table A1). The median basin size resulting from basin delineation B is 114 km², with a range of 1 to 2 500 km². Significant reduction of polygon size at the upper end ensures a more representative mapping of local features.

The third basin delineation provided in LamaH (further referred to as basin delineation C in the text and dataset) is similar to

135 basin delineation B, but only includes catchments with no or only low anthropogenic influence (454 catchments; Fig. 2c). This provides a bundled collection of catchments that exhibit hydrological conditions that are close to natural ones. Anthropogenic influences in the catchments and runoff data is described more detailed in section 5.8.
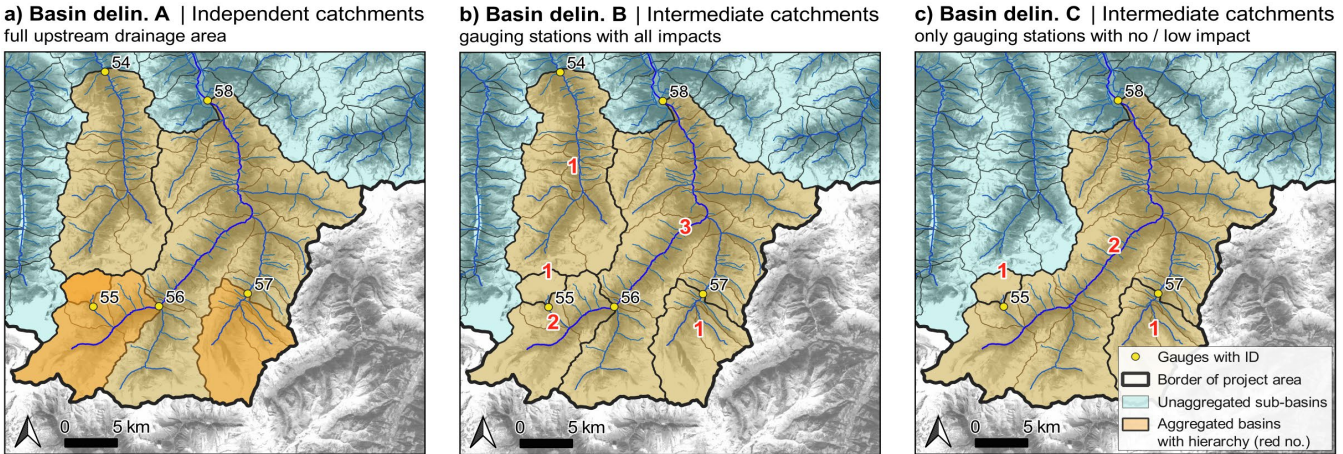
140 Fig. 2: Types of basin delineations in LamaH shown with an example. Plot a) Basin delineation A (similar to the well-known CAMELS datasets): The aggregation area corresponds to the topographic catchment area of a gauge. In plot a), the aggregation area of gauges 56 and 57 overlaps with that of gauge 58, and the aggregation area of gauge 55 overlaps with that of gauges 56 and 58 (indicated by the different color tones). Plot b) Basin delineation B: The aggregation areas in this method considers the difference

145 area (intermediate catchments) between the topographic catchment area of the respective gauge and the catchment area of the next upstream gauges. Consequently, there are no overlaps, but a gauge hierarchy is necessary. The hierarchy of the gauges 54, 55 and 57 is 1, because there is no upstream gauge. Gauge 56 has the hierarchy 2, because gauge 55 with hierarchy 1 is upstream. Hierarchy 3 is assigned to gauge 58, because there is at least one gauge with hierarchy 2 (gauge 56) in the upstream area. Plot c) Basin delineation C: Similar to basin delineation B, but only uninfluenced or low-influenced gauges / catchments (section 5.8) are considered. In plot c), it is assumed that gauges 54 and 56 are strongly influenced. Consequently, these two gauges are excluded from the basin

150 delineation. The aggregation area of gauge 58 (now hierarchy 2) includes the intermediate catchment area of gauge 56. Source of background satellite image: Google © 2020 TerraMetrics, Kartendaten © 2020. Source of stream network: TYROL (2020).

Aggregation of the spatially distributed information of the used basic datasets for meteorological time series and various static attributes is performed for each of the 3 basin delineations by calculating the area-weighted arithmetic mean (otherwise indicated in the text). This method of aggregation is used for coarser gridded and vectoral data sources and is referred in the

155 following as "upscaling approach 1". The alternative "upscaling approach 2" is based on all the raster cells, which centroids are located inside the polygon ("aggregated basins" in Fig. 2). In case of small catchments, where no or only one raster centroid intersects the polygon, upscaling approach 1 was used. Upscaling approach 2 is mainly used for relatively fine-gridded data sources (< 1 km grid size), since it is not that computing-intensive and potential inaccuracies are negligible. The applied approach is indicated in the relevant tables in appendix A.

160 **4 Hydrometeorological time series**

4.1 Runoff data

LamaH contains daily and hourly runoff time series for 882 gauges, located in 4 countries (Austria, Germany, Switzerland and Czech Republic). The difference to the 859 catchments defined in basin delineation A (section 3) can be explained by the fact that 23 gauges, which mostly do not have a clearly definable catchment area (e.g. gauges at artificial channels or below large

165 karst springs; section 5.8), were not considered in basin delineation. The main provider of runoff time series was the Hydrographic Central Bureau of Austria (HZB, 2020), which contributed data for 609 gauges located in Austria. The hydrographical services of the German federal states Bavaria (GKD, 2020) and Baden-Württemberg (LUBW, 2020) provided 125 and 61 runoff time series, respectively. 25 runoff time series came from the hydrological office of Switzerland (BAFU, 2020), while time series for 61 gauges were provided by the Czech Hydrometeorological Institute (CHMI, 2020). The format

170 of all obtained time series was unified, enabling much easier data processing. The various gauge attributes and metadata are listed and described in Table A1. The unit of discharge is $m^3 \, s^{-1}$ for both daily and hourly resolution. Conversion to runoff heights can be performed using the catchment area provided ("area_gov" in Table A1 or "area_calc" in Table A3).

Runoff time series are in most cases derived by water level - discharge relationships (rating curves). Changes in channel profile, e.g. after floods with strong bedload transport, extrapolation of the rating curve or backwater effects and transient runoff

175 conditions (runoff hysteresis) can lead to an incorrect runoff determination (McMillan et al., 2012). However, attempts are usually made to minimize this source of error by periodically adjusting the rating curve. The adjustment frequency of these

rating curves is not publicly available, but only gauges in the highest quality class (quality classes are declared in Bavaria and the Czech Republic) were included in LamaH.

Runoff time series with daily resolution are often provided with longer observation periods than those with hourly resolution. Therefore, daily and hourly runoff time series can be obtained separately from the listed hydrological offices. However, we normally requested only the time series with hourly resolution and derived the daily time series from them. Thereby the hourly values of the respective day were used for determining the daily values (as well as for the meteorological variables), e.g. for 1 October 1981: 1 October 1981 00:00 to 1 October 1981 23:59 GMT. This approach was chosen for the runoff data from Austria, Germany and Switzerland, since those time series with hourly resolution mostly include quite long recording periods. Fig. 3a and the included histogram show that most gauges have continuous data recording since the late 1970`s. In contrast, the time series from the Czech Republic were requested with both daily and hourly resolution, as the continuous (hourly) time series here only starts after 2005. The runoff time series in LamaH were limited to the period 1981 to 2017, because 1981 was the starting year of the meteorological ERA5-Land forcings (section 4.2), and 2017 was the last year for quality-controlled runoff data from Austria at the point of request.

Although the exact scope of data verification by the staff of the various hydrological services is not further specified, we have added an attribute describing the check status ("ckhs" in Table A1) to each time step of the runoff time series. The Austrian, Czech and Swiss runoff data are provided exclusively checked, while the runoff data from the Bavarian hydrographic service is in most cases quality controlled until the years 2014 / 2016. Data from the German federal state Baden-Württemberg is often checked only from the year 2010 onwards. Some time series included gaps, even after checking by the hydrological services ("gaps_pre" in Table A1). Gaps of up to 6 hours were filled with linear interpolation during our processing, if the number of consecutive gaps was less than 7. Any remaining gaps (> 6h) were marked with the number -999. The fraction of remaining gaps in the continuous runoff time series is declared by the attribute "gaps_post" and illustrated in Fig. 3b. It is shown that those gauges with very few gaps (< 0.1‰) are mostly located in Austria, Czech Republic and Switzerland. About 80% of the 882 gauges have no gaps in their continuous time series after our processing. The time steps with gaps before our processing are listed in separate files, attached to the dataset. The spatial distribution of the gauge hierarchy (see caption of Fig. 2b) is mapped in Fig. 3c., where 50% of all gauges have a hierarchy of 1. The highest hierarchy (26) is found for the very last downstream gauge of the Austrian Danube (ID 399). Lastly, the attributes "nrs_euhyd" and "nrs_rivat" allow cross-references to the river network datasets EU-Hydro-River Network Database (EEA, 2019) and RiverATLAS (Linke et al., 2019), respectively. Thereby the ID of the corresponding river section to the gauge is given, enabling access to their attributes and routing through these networks.
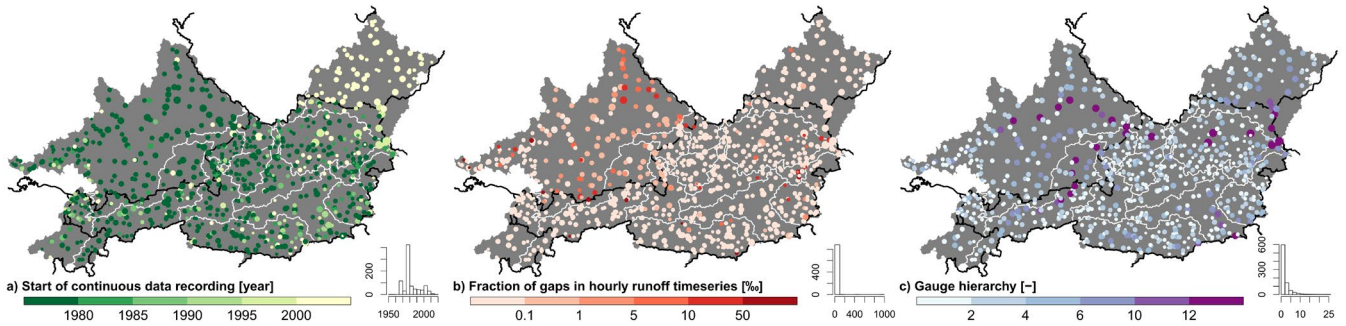
Fig. 3: Maps showing a selection of gauge-referenced attributes. The size of the circles is proportional to the respective catchment area. The histograms indicate the number of gauges (out of 859) in each category. © EuroGeographics for the administrative boundaries.

4.2 Meteorological data

Given the extent of the ECMWF (European Centre for Medium-Range Weather Forecasts) ERA5-Land dataset with global coverage (Muñoz Sabater et al., 2021), it was possible to obtain gap-free time series with daily and hourly resolution for 15 meteorological variables and 39 years (Table A2). ERA5-Land is a derivative of the ERA5 climate reanalysis (Hersbach et al., 2020), but only covers the terrestrial components. Further developments compared to ERA5 include an interpolation package for a finer temporal resolution, an additional sea level adjustment of the meteorological fields, as well as more efficient possibilities for the import of updates (Muñoz Sabater et al., 2021; Yang and Giusti, 2020). ERA5-Land has a spatial resolution of 0.1 arc degrees (about 9 x 11 km at the latitudes of the project area) compared to the grid size of ERA5 of 0.25 arc degrees. The temporal resolution of ERA5-Land is 1 hour, while ERA5 only has a 3-hour resolution. There is no data assimilation (fitting to observations) applied for ERA5-Land, but observations are indirectly implemented via the assimilated atmospheric fields of ERA5 (Hennermann and Guillory, 2020; Yang and Giusti, 2020). In accordance to ECMWF regulations, an uncertainty estimate for ERA5-Land will be released (Muñoz Sabater, 2019b; Muñoz Sabater et al., 2017), but was not available at the time of writing (January 2021).

Meteorological time series were computed for all 3 forms of basin delineation (A/B/C in section 3). The aggregation was done by calculating the area-weighted arithmetic mean (upscaling approach 1). As already mentioned in the introduction, we would like to point out possible uncertainties of the published data. We therefore determined the components of the water balance for the period 1 October 1989 to 30 September 2009 (hydrological years 1990 to 2009) and plotted them (Fig. 4a). Values of catchments influenced by cross-basin water transfers, water withdrawals or intakes, large karstic springs or high infiltration (section 5.8) are not shown in Fig. 4a/c to allow a more objective interpretation. In case of long-term water balances, it is usually feasible to neglect artificial storage in the catchment. The difference between long-term mean precipitation (P) and runoff height (Q), as recorded at the gauging station, should be equal to the total evapotranspiration (ETA) in a fulfilled water balance. This would be shown by having all points in Fig. 4a on the 1:1 line, which is not the case. Reasons for the rather strong scatter (Pearson correlation R = 0.30) may be an insufficient representation of precipitation or total evapotranspiration by ERA5-Land, an inaccurate recording of runoff (e.g. strong, unrecorded groundwater flow or change in river profile at the

gauging station and thus inadequate water level - discharge relationship), a significant deviation between topographic and hydrographic catchment area (subsurface inflows and outflows, especially in karstic areas), or lastly, in case of existing glaciers, a negative mass balance (Lambrecht and Kuhn, 2007; Kuhn, 2004; Kobolschnig and Schöner, 2011; Oerlemans et al., 1998; WGMS, 2005). Using other precipitation datasets for the same evaluation does not result in a significantly more compliant long-term water balance. CHIRPS Daily v2 (Funk et al., 2015) resulted in a correlation R between (P - Q) and ETA
240   of 0.34 or MSWEP v2.2 (Beck et al., 2017; 2019) in even a lower R-value of 0.26. Even if we cannot resolve the issue at hand, the total evapotranspiration from ERA5-Land and its dependence on elevation seems quite plausible compared to other studies (Fig. 4a; HAO, 2007, Map 3.3; Herrnegger et al., 2012, Fig. 20). Negative differences of mean precipitation and runoff height (Fig. 4a) and thus runoff coefficients > 1.0 (Fig. 4c, 32 of 594 catchments) are mainly present in higher terrain (negative mass balance of glaciers, Fig. 8d) and in catchments with a high fraction of carbonate sedimentary rocks (indicator of karst, Fig.
245   11c). Since ERA5-Land indirectly incorporates in-situ observational data via the assimilated atmospheric fields of ERA5 (Yang and Giusti, 2020), systematic measuring error of a terrestrial station being used could explain insufficient mean precipitation (Herrnegger et al., 2018). The individual components of the water balance are attached to the dataset for every catchment (Table A10), since this evaluation might be useful for explaining any deviations in a later modelling.

The Budyko curve (Fig. 4b; Budyko 1974) describes the relationship between the ratio current evapotranspiration /
250   precipitation (ETA/P) and the ratio potential evapotranspiration / precipitation (PET/P) and indicates whether evapotranspiration of a catchment is limited by energy or water. Ideally all points should lie in the proximity of the Budyko curve. The deviation from this ideal case can primarily be explained by a significantly too high PET of ERA5-Land over nearly the entire range of elevation. For example, 98% of all 859 watersheds show mean annual PET sums above 1000 mm ("PET" in Table A10). As these PET sums are not realistic at the latitudes of the project area (HAO, 2007, Map 3.2; Herrnegger et al.,
255   2012, Fig. 17), we did not include PET time series of ERA5-Land in the LamaH dataset. However, there is the possibility to obtain daily PET time series from provided fluxes of the hydrological model (section 6; Table C2). The runoff coefficient (Q/P) as a function of the ratio mean precipitation / total evapotranspiration (P/ETA) is shown in Fig. 4c. The altitudinal dependency can be clearly seen in Fig. 4c, while catchments with lower mean elevation show less scatter. Fig. 4d shows the contrast of the long-term precipitation of ERA5-Land with those of ERA5 (Pearson correlation R = 0.936). ERA5 indicates
260   systematic surplus of precipitation at catchments with mean altitudes above 2000 m a.s.l. compared to ERA5-Land, while at catchments with mean altitudes between 800 and 1200 m a.s.l. the opposite is more likely to be the case. The correlation between the long-term precipitation of ERA5-Land and those of the dataset CHIRPS daily v2 (Funk et al., 2015) is 0.916 (Fig. 4e). Further, the mean precipitation sums of CHIRPS daily v2 tend to be lower than those of ERA5-Land over the whole range of altitudes. More scatter (R = 0.841) appears especially in catchments with higher elevations when comparing the long-term
265   precipitation sums of ERA5-Land and MSWEP v2.2 (Beck et al., 2017; 2019; Fig. 4f).
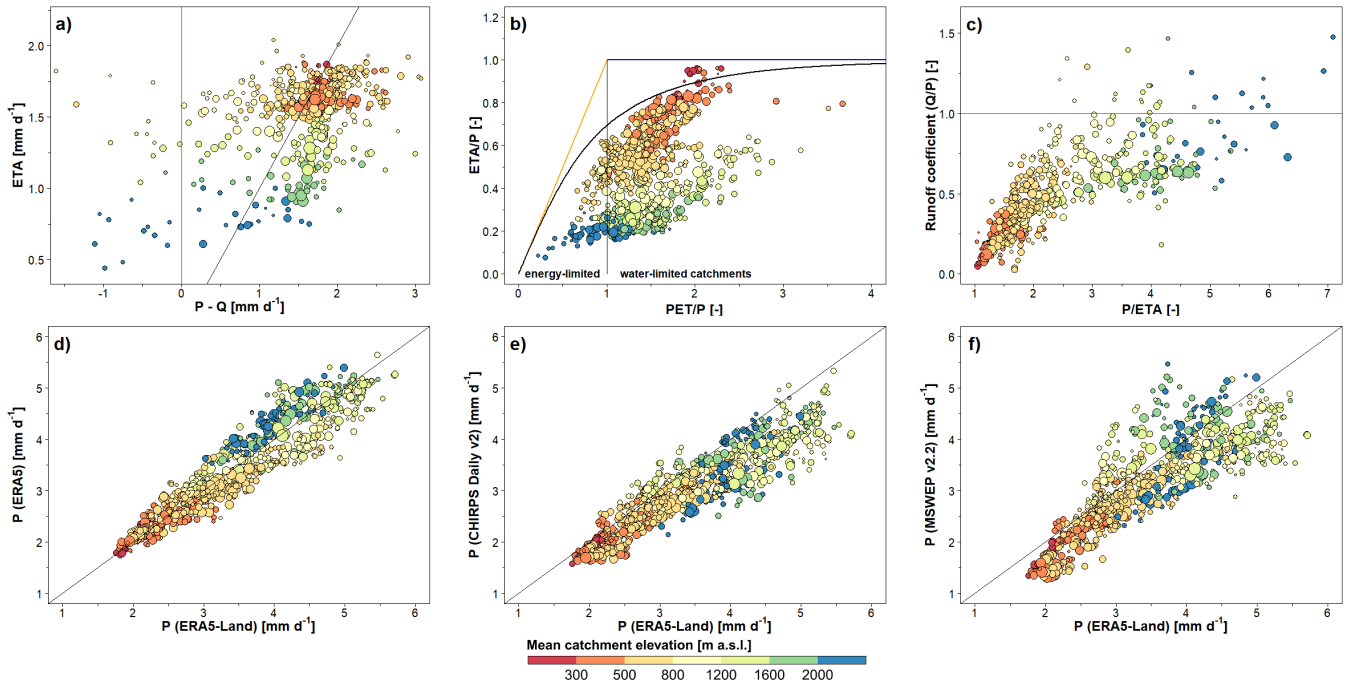
Fig. 4: Analysis regarding the long-term water balance, evapotranspiration and comparison of the ERA5-Land`s mean precipitation with other datasets for the hydrological years 1990 - 2009 and basin delineation A. a) Total evapotranspiration (ETA) from ERA5-Land as a function of the difference between precipitation (P) from ERA5-Land and recorded runoff depth (Q). b) Budyko curve indicates if ET of a catchment is limited by energy (PET/P < 1) or by water (PET/P > 1). c) shows the runoff coefficient (ratio of Q and P) as a function of the fraction of ERA5-Land´s precipitation and total evapotranspiration. In a), b) and c), values are only plotted for basins with observations for the period 1 October 1989 to 30 September 2009 (717 basins). Further, in a) and c), values are only plotted for basins not affected by artificial water input or withdrawal, karstic springs or high infiltration (594 basins; section 5.8). Plots d) / e) and f) illustrates the relationship between ERA5-Land´s precipitation compared to the datasets "ERA5", "CHIRPS Daily v2.0" and "MSWEP v2.2" in 859 catchments. The diagonal black line in a), d), e) and f) is the 1:1 line. The red lines in a) and c) show physical constraints. The sloped orange line in b) indicates the energy-limit, while the horizontal blue line represents the water-limit. The curved black line in b) represents the Budyko curve. The size of the symbols in all plots is proportional to the catchment area, while the color indicates the mean elevation of the catchment (see legend at bottom).

5 Catchment attributes

The various physio-geographical characteristics of a catchment, as well as their interactions, are essential for water storage and transport on and below earth's surface (Blöschl et al., 2013). The spectrum of influencing catchment characteristics includes topography, climate, hydrology, land cover, vegetation, soil, geology, as well as the type and degree of (anthropogenic) impact on runoff processes. Furthermore, catchment attributes are crucial to determine interrelationships among different watersheds along several gradients (Addor et al., 2017a; Falkenmark and Chapman, 1989; Fan et al., 2019).

In most cases, we used freely available datasets with global or at least European coverage for deriving the different catchment attributes. The used datasets for deriving the attributes, methods of processing, possible uncertainties as well as the spatial distribution of catchment attributes (Addor, 2017b) are discussed in more detail in the following subsections. It is clear that

due to the large dataset this account is far from complete. The individual attributes are listed in tabular form in the appendix with a more detailed description, units and with reference to the data sources.

5.1 Topographic indices

We calculated 10 topographic attributes, which are listened in Table A3. The attribute "area_calc" describes the calculated aggregation (catchment) area, depending on the applied method of basin delineation (section 3). A key factor for hydrologic processes is elevation, as it affects numerous other catchment characteristics including climate, land cover, vegetation, or soil development (Addor et al., 2017a). We derived the mean catchment elevation (Fig. 5b, "elev_mean" in Table A3), the median elevation ("elev_med"), standard deviation within a catchment ("elev_std"), the elevation range (maximum-minimum elevation in the catchment, Fig. 5c, "elev_ran"), as well as the mean catchment slope (Fig. 5d, "slope_mean") from NASA's SRTM dataset (Farr et al., 2007). SRTM features a grid size of 30 m and provides a maximum global absolute vertical error of 16 m at a 90% confidence interval, while accuracy decreases with increasing elevation and slope (Farr et al., 2007). The slope was calculated with the algorithm of Horn (1981) using the terrain elevation from SRTM. High mean catchment elevations and slopes are most apparent in the Eastern Alps, which extend from the southwest to the central east of the project area. This high elevated area is mainly surrounded by the flatter Alpine foothills and regions with older geological zones (Fig. 5b).

The shape of the catchment area and the stream network influence runoff formation. The direction of precipitation in relation to the longitudinal axis of the catchment is of major interest in case of flood situations, especially in larger catchments. For this reason, we specified the angle between the north direction and the longitudinal axis ("mvert_ang") in addition to the distance of the longitudinal axis of a catchment ("mvert_dist"). In combination with the two wind components of ERA5-Land ("10m_wind_u", "10m_wind_v" in Table A2) it is possible to derive the relative rainfall trajectory. Furthermore, the catchment shape is relevant for the rise of the flood wave. The attribute of length elongation according to Schumm (1956) (Fig. 5e, "elon_ratio") is an indicator regarding the "roundness" (the higher, the rounder) of the catchment. Stream density (Fig. 5f, "strm_dens") is a function of several characteristics (e.g. climate, relief, soil properties, geology, vegetation, land use, glaciation or karstification) and can therefore be an informative indicator for comparing watersheds (Olden and Poff, 2003). The EU-Hydro – River Network Database (EEA, 2019) is used for calculating the stream density, since it is a fine-resolved dataset and consistent over the covered project area.
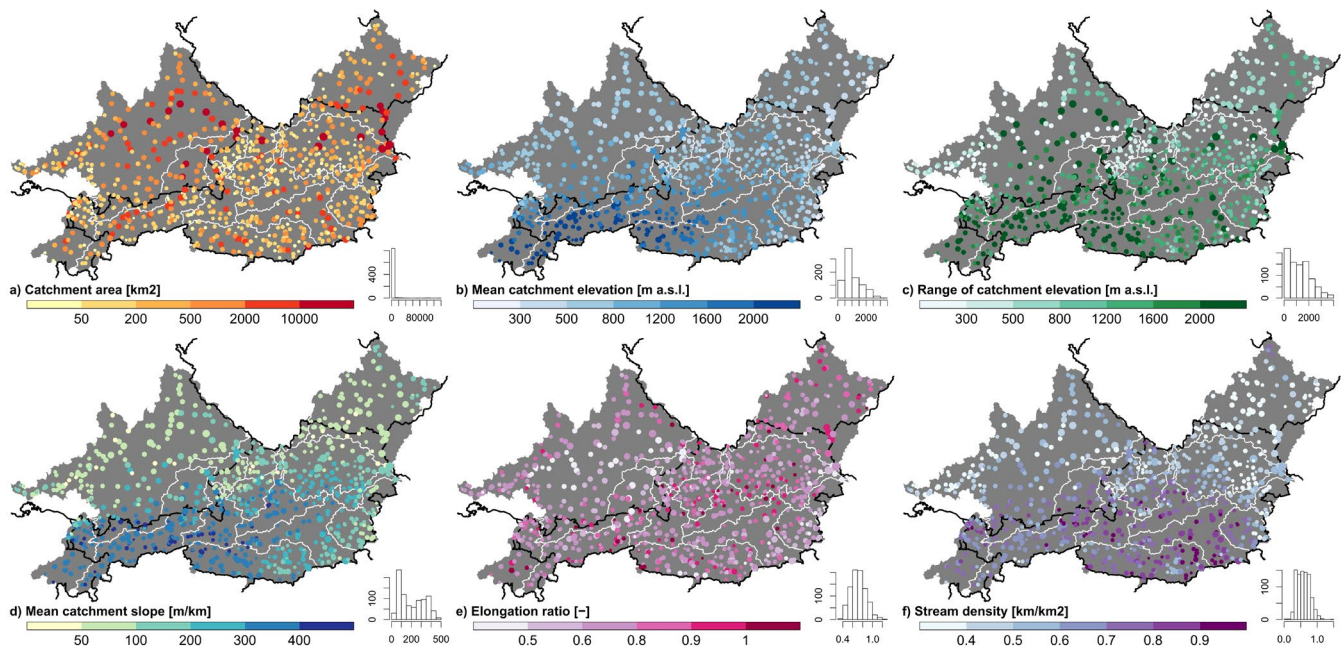
Fig. 5: Spatial distribution of a selection of topographic attributes representing the characteristics of the entire topographic catchment (basin delineation A, Fig. 2a). The histograms indicate the number of basins (out of 859) in each category. The size of the circles is proportional to the catchment area. © EuroGeographics for the administrative boundaries.

5.2 Climatic indices

LamaH includes 12 attributes reflecting aspects of climatic characteristics (Table A4). These attributes were calculated mainly from the meteorological time series of ERA5-Land for the period 1 October 1989 to 30 September 2009 (Addor, 2017b). The Reference Evapotranspiration (ET0) from the "Global Aridity Index and Potential Evapotranspiration (ET0) Climate Database v2" (GCD v2; Trabucco and Zomer, 2019), which was computed for the period 1970 to 2000 is provided as an alternative to ERA5-Land´s potential evapotranspiration, which shows unrealistic high values (section 4.2). ET0 describes the atmosphere's capacity for evapotranspiration given defined vegetation characteristics. Potential evapotranspiration (PET) can be derived from ET0 using correction factors for vegetation and soil properties (Allen et al., 1998; Hargreaves, 1994), but was not realized in LamaH.

Long-term climatic characteristics are described by long-term daily precipitation (Fig. 6a, "p_mean" in Table A4), reference evapotranspiration (Fig. 6b, "et0_mean"), total evapotranspiration ("eta_mean"), and the aridity index (Fig. 6c, "arid_2"). As an alternative, the aridity index which was calculated by dividing ET0 from GCD v2 and precipitation from ERA5-Land is also included ("arid_1"). The spatial pattern of long-term precipitation sums (Fig. 6a) clearly shows an elevation gradient and blocking effects along the northern Alps. The west of the project area is characterized by higher mean precipitation due to the stronger influence of oceanic climate. The relationship between mean catchment elevation (Fig. 5b) and ET0 (Fig. 6b, Pearson correlation R = -0.79), aridity (Fig. 6c, R = -0.68), or the fraction of precipitation falling as snow (Fig. 6g, R = 0.96) show

similar spatial patterns. About 19% of all catchments, which are exclusively located in the eastern part of the project area, have

335   aridity greater than 1 ("arid_2").

Attributes characterizing seasonality are the fraction of precipitation falling as snow (Fig. 6g, "frac_snow") and the seasonality index, which relies on sinusoids to describe the precipitation cycle over the year (Fig. 6d, "p_season"). A higher positive seasonality index indicates higher precipitation sums during summer, while values near 0 show a more balanced precipitation distribution throughout the year.

340   While long-term and seasonal indices describe general climatology, they provide little or no information about relatively short-term events such as drought or heavy rainfall. Consequently, we calculated attributes representing the frequency of high precipitation days (days per year with at least 5 times mean daily precipitation; Fig. 6e, "hi_prec_fr") and dry days (days per year with max. 1 mm d^{-1} precipitation; Fig. 6h, "lo_prec_fr"), their mean duration (Fig. 6f, "hi_prec_du" / Fig. 6i, "lo_prec_du"), and the most likely season of occurrence ("hi_prec_ti" / "lo_prec_ti"). The reason for the higher frequency of

345   high precipitation days in the south-eastern part of the project area (Fig. 6e) is primarily the combination of relatively rainfall-rich convective precipitation events during the summer months and relatively low precipitation sums during the rest of the year (Fig. 6d). For both, the mean frequency of dry days (Fig. 6h, R = -0.62) as well as their mean duration (Fig. 6i, R = -0.57), a negative spatial correlation with the mean catchment elevation (Fig. 5b) can be observed. Most common season for high precipitation is for 89% of all 859 catchments summer (June, July and August), while winter (December, January and February)

350   is the most common season for dry days in 89% of the basins.
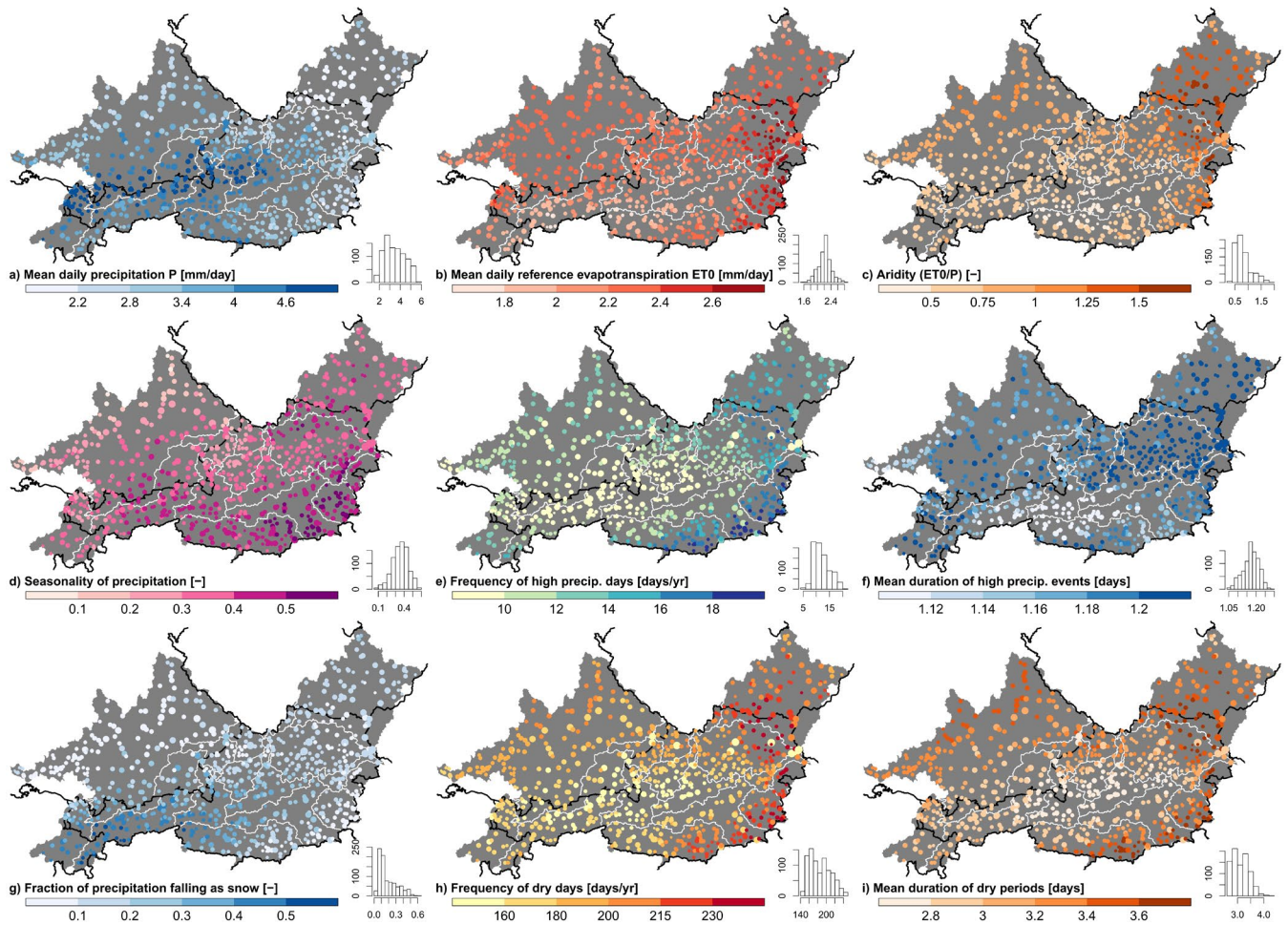
Fig. 6: Spatial distribution of a selection of climate indices representing the characteristics of the entire topographic catchment (basin delineation A, Fig. 2a). The histograms indicate the number of basins (out of 859) in each category. The size of the circles is proportional to the catchment area. © EuroGeographics for the administrative boundaries.

5.3 Hydrological signatures

The runoff time series are characterized by 14 attributes (Table A5) which were calculated for the period 1 October 1989 to 30 September 2009 (Addor, 2017b). The indices were computed for those gauges which cover the whole period of investigation (717 gauges). However, evaluations for the entire period of record (first 1 October after 1981 to 30 September 2017) are additionally made available if at least 5 full hydrological years are recorded. 4 gauges do not meet this requirement. Hydrological signatures are calculated, only if the fraction of gaps is less than 5% for both evaluation periods. Hydrological attributes can be divided into those describing long-term characteristics, seasonality, and more short-term situations such as high and low flow.

Aridity by itself can be a good predictor for runoff occurrence in a catchment (Arora, 2002; Blöschl et al., 2013; Budyko, 1974). This is shown by the similar spatial pattern of long-term runoff height (Fig. 7a, "q_mean" in Table A5, R = -0.61), and

runoff ratio (Fig. 7b, "runoff_ratio", R = -0.60) compared to those of aridity (Fig. 6c). The runoff coefficient (Q/P) is the fraction of precipitation that drains a surface after deducting evapotranspiration, groundwater flow or change in storage in the long-term. Explanations for runoff coefficients greater than 1 are given in section 4.2. The ratio of baseflow and total runoff can be a useful indicator for watershed classification (Sawicz et al., 2011; Fan, 2015), and is further referred as the baseflow index ("baseflow_index"). It should be noted that this index is highly dependent on the method used to separate the hydrograph (Beck et al., 2013; Chapman, 1999; Eckhardt, 2008). For this reason, we used the Ladson filter (Ladson et al., 2013) and the approach of Tallaksen and Van Lanen (2004) for hydrograph separation. The runoff-precipitation elasticity ("stream_elas") characterizes the inertia of change in mean runoff given a change in mean precipitation (Sankarasubramanian et al., 2001). For example, a value of 3 would indicate a change in runoff of 3% given a change in precipitation of 1%. High runoff-precipitation elasticity is especially present in the eastern part of the project area (Fig. 7f). The fraction of days without discharge (not shown, "zero_q_freq") may indicate strong infiltration (e.g. Danube Sinkhole; Hötzl, 1996), artificial water withdrawal, or ceasing baseflow.

The seasonality of runoff is expressed by the attribute "hfd_mean", which shows the number of days from the beginning of the hydrologic year (1 October) to the date when half annual of the runoff volume is reached (Court, 1962). Higher number of days in Fig. 7c can be explained primarily by water storage in form of snow (Fig. 6g) or glaciers (Fig. 8d). Variability in runoff (Fig. 7d, "slope_fdc") is expressed within LamaH by the slope of the flow duration curve between the log-transformed 33rd and 66th runoff percentiles (Sawicz et al., 2011). High values are indicative for high runoff variability over the year, which can be caused by seasonal water storage in the form of snow (Fig. 6g) or a strong response of runoff to precipitation (Yokoo and Sivapalan, 2011). Extreme runoff events such as high or low flow are described by indices representing mean frequency (Fig. 7g, "high_q_freq" / Fig. 7j, "low_q_freq"), duration (Fig. 7h, "high_q_dur" / Fig. 7k, "low_q_dur") and magnitude. The threshold for high flow (at least 9 times median daily discharge) is chosen according to Clausen and Biggs (2000), and that for low flow (max. 0.2 times median daily discharge) according to Olden and Poff (2003). The magnitudes of extreme flows are expressed by the 95th (high flow, Fig. 7i, "Q_{95}") and the 5th (low flow, Fig. 7l, "Q_5") runoff percentiles. The hydrological indices (Fig. 7) are spatially less smoothly distributed compared to the climatic indices (Fig. 6). The reasons might be the influence of the (non-) linear hydrological processes by locally heterogeneous catchment characteristics or uncertainties in runoff measurement (Addor et al., 2017a; Westerberg et al., 2016).
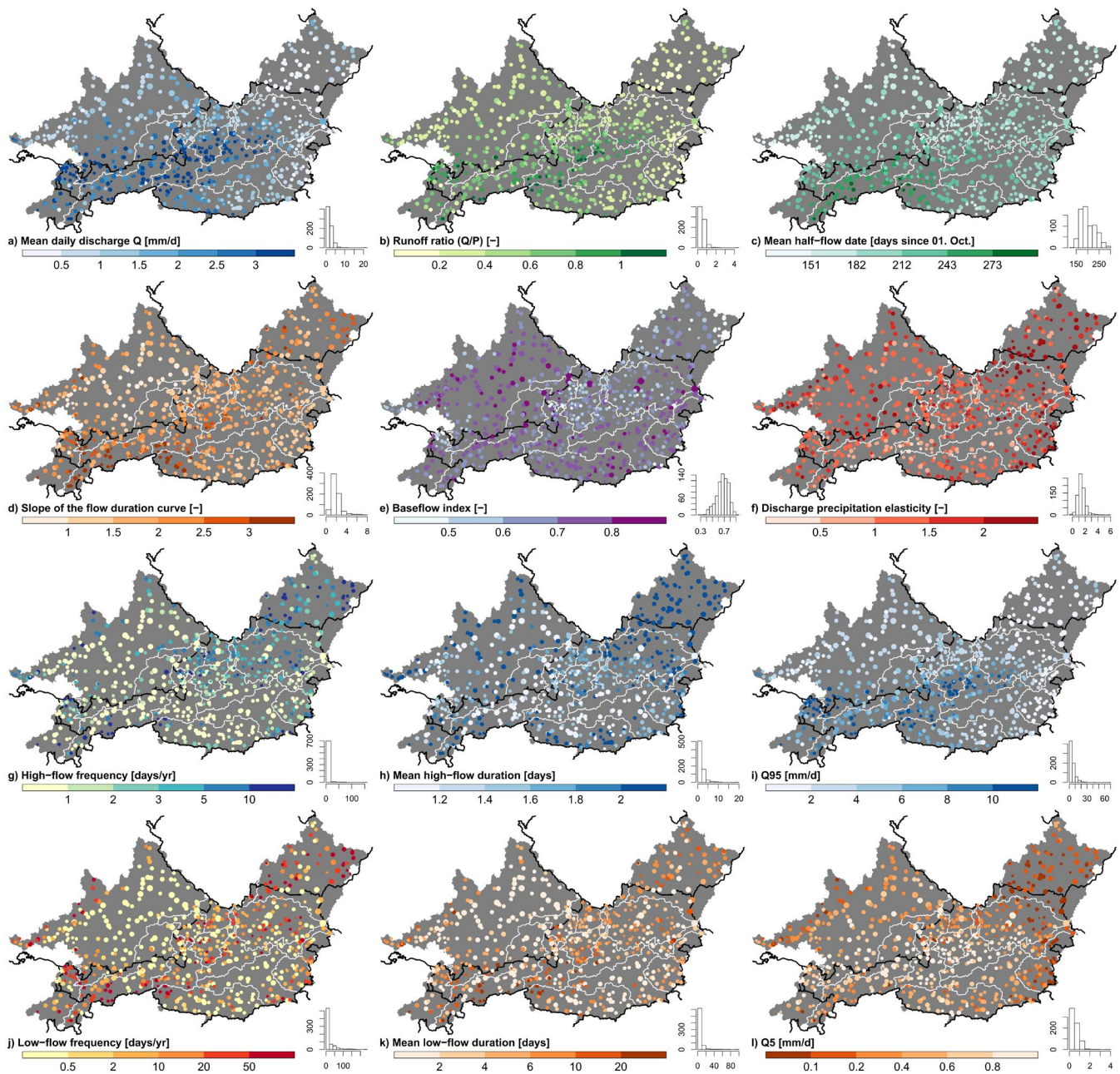
Fig. 7: Spatial distribution of hydrological signatures. Only gauges are plotted, which cover the period 1 October 1989 to 30 September 2009. The histograms indicate the number of gauges (out of 717) in each category. The size of the circles is proportional to the catchment area. © EuroGeographics for the administrative boundaries.

5.4 Land cover characteristics

All attributes concerning land class (Table A6) are based on the CORINE Land Cover (CLC) 2012 raster dataset featuring a grid-size of 100 m (CORINE, 2012). CORINE is an initiative of the European Environment Agency with the aim to record

land cover of the European territory with a 6-year update cycle. The basic technical specifications like 44 land classes, 25 hectares minimum mapping unit (MMU) for areal phenomena and 100 m minimum width for linear phenomena have not changed since the beginning, facilitating comparisons over the years (CORINE, 2012). It should be noted that an MMU of 25 hectares prevents mapping of very small scaled structures. Other limitations might be the variability of satellite image quality and contents, difficulties for setting up automatic conversion processes, the difference between human interpretation capacity and pixel-based classification (Bossard et al., 2000). However, the total reliability of the predecessor dataset CLC 2000 is 87.0 ± 0.8% according to a reinterpretation approach. The worst class-level reliability (< 70%) was found for sparse vegetation (CLC class 333) (Büttner and Maucha, 2006). The dominant land class within a basin delineation is derived by the majority of the intersecting raster centroids, while the fractions are derived by area share of the specific raster cells.

Agricultural land (Fig. 8a, "agr_fra" in Table A6) has high fractions in catchments with low mean slope (Fig. 5d, R = -0.89). The opposite occurs for fraction of bare areas (Fig. 8b, "bare_fra"), since the vegetation period is very short at high elevated terrain and a high terrain slope fosters gravitational erosion processes. Following the CAMELS datasets, no differentiation was made between deciduous and coniferous forests when calculating the forest share. The proportion of forest is highest in the central-eastern region of the project area (Fig. 8c, "forest_fra"), where agriculture and settlement are less prevalent and the mountains are often lower than the forest line. Catchments with a relatively high proportion of glaciers (Fig. 8d, "glac_fra") are mainly located in the western Eastern Alps. The influence of glaciers upon the hydrological regime is primarily apparent in the upper parts of the river regions Inn (region 3 in Fig. 1 and Table B1), Salzach (region 4) and Drava (region 18). High proportions of water surface (Fig. 8e, "lake_fra") can be explained by large lakes, which were mostly formed at the end of the last great ice age about 10 000 years ago (mainly in the Alpine foothills), or by large artificial water reservoirs (mainly in the Czech Republic). Catchments in the Vienna metropolitan area (eastern part of river region 10), as well as in the lower Rhine valley (northern part of river region 1) show quite high fractions of urban area (Fig. 8f, "urban_fra"). However, most catchments (about 74%) have less than 5% urban area.
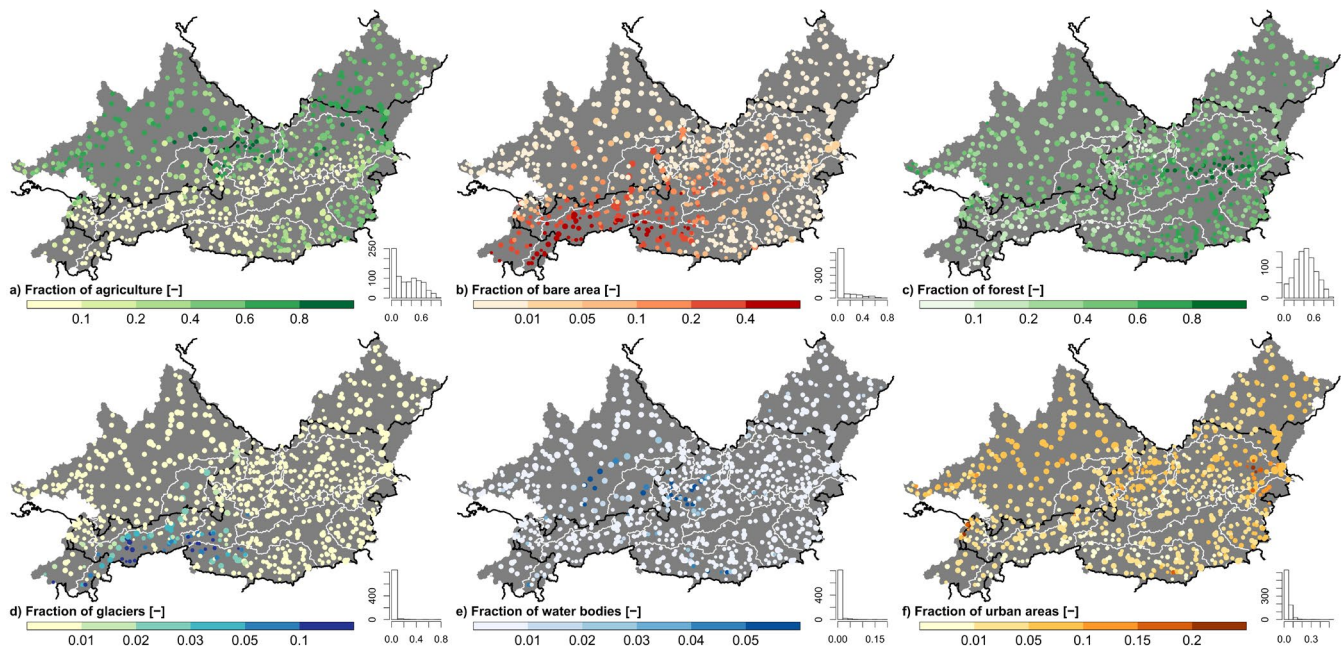
Fig. 8: Spatial distribution of land class fractions representing the characteristics of the entire topographic catchment (basin delineation A, Fig. 2a). The histograms indicate the number of basins (out of 859) in each category. The size of the circles is proportional to the catchment area. © EuroGeographics for the administrative boundaries.

5.5 Vegetation indices

We calculated 6 catchment attributes describing vegetation indices, which are based on Leaf Area Index (LAI), Normalized Difference Vegetation Index (NDVI), and Green Vegetation Fraction (GVF) (Table A7). All vegetation indices are based on long-term monthly means, using either the maximum, minimum, or difference between the maximum and minimum monthly means (based on 12 monthly means). Processing of the remote sensing datasets was done using the Google Earth Engine platform (GEEa, 2021; GEEb, 2021; Gorelick et al., 2017).

LAI represents vertical vegetation density and is defined as the sum of one-sided green leaf area per unit area for deciduous forests and half of the total needle area per unit area for coniferous forests. LAI was derived from the "MODIS MCD15A3H" dataset, which is a 4-day composition with 500 m grid resolution (Myneni et al., 2015). The maximum and minimum monthly means were calculated for the period 1 August 2002 to 1 January 2020 using a cloud filter. The maximum monthly mean of LAI (Fig. 9a, "lai_max" in Table A7) and the difference between maximum and minimum (Fig. 9d, "lai_diff") show a spatial correlation with the forest fraction (Fig. 8c, R = 0.76 respectively 0.75). LAI$_{diff}$ shows the same values as LAI$_{max}$ for large parts of the project area. Especially in regions characterized by a high proportion of coniferous forest the LAI$_{diff}$ should be smaller than LAI$_{max}$ due to the permanent green cover. Snow cover during the winter months could be a possible reason for the non-representative measurement of the minimum values of LAI.

NDVI is derived from the backscatter of 2 spectral bands and is widely used for remote sensing-based vegetation monitoring and classification (horizontal density, type, and physiological condition). The maximum and minimum monthly NDVI is based

on the "MODIS MOD09Q1" dataset with a temporal resolution of 8 days and a spatial resolution of 250 m (Vermote, 2015). The calculation was performed for the period 1 April 2000 to 1 January 2020, applying a filter on cloudy satellite images. A negative correlation is apparent between the $NDVI_{max}$ (Fig. 9b, "ndvi_max", R = -0.78) or the $NDVI_{min}$ (Fig. 9e, "ndvi_min", R = -0.84) and the mean catchment elevation (Fig. 5b).

445 GVF (Green Vegetation Fraction) indicates the fraction of soil that is covered by green vegetation and can be derived from the NDVI as follows in Eq. (1) (Broxton et al., 2014):

$$GVF = \frac{NDVI - NDVI_s}{NDVI_{c,v} - NDVI_s} \quad (1)$$

where NDVI represents the (maximum or minimum) monthly mean of NDVI, $NDVI_s$ the annual maximum NDVI of bare ground, and $NDVI_{c,v}$ the annual maximum of vegetated ground surface as a function of IGBP land class (Table 1 in Broxton et al., 2014). $NDVI_s$ was set to 0.09 in accordance to Broxton et al. (2014), while the spatial distribution of the IGBP land

450 classes was obtained from the "MODIS MCD12Q1" dataset of the year 2012 (Friedl and Sulla-Menashe, 2019). As the values for $NDVI_s$ and $NDVI_{c,v}$ were derived for a global scale and thus do not necessarily correspond to conditions in the project area, it is possible for GVF values to exceed the normal range between 0 and 1. In order to maintain consistency, we did not constrain the GVF to the normal range, however. The spatial distribution of GVF_{max} (Fig. 9c, "gvf_max") shows similar spatial patterns to those of LAI_{max} (R = 0.79) as well as $NDVI_{max}$ (R = 0.94), while GVF_{diff} (Fig. 9f, "gfv_diff") tends to be higher in regions

455 with a higher fraction of precipitation falling as snow (Fig. 6g).
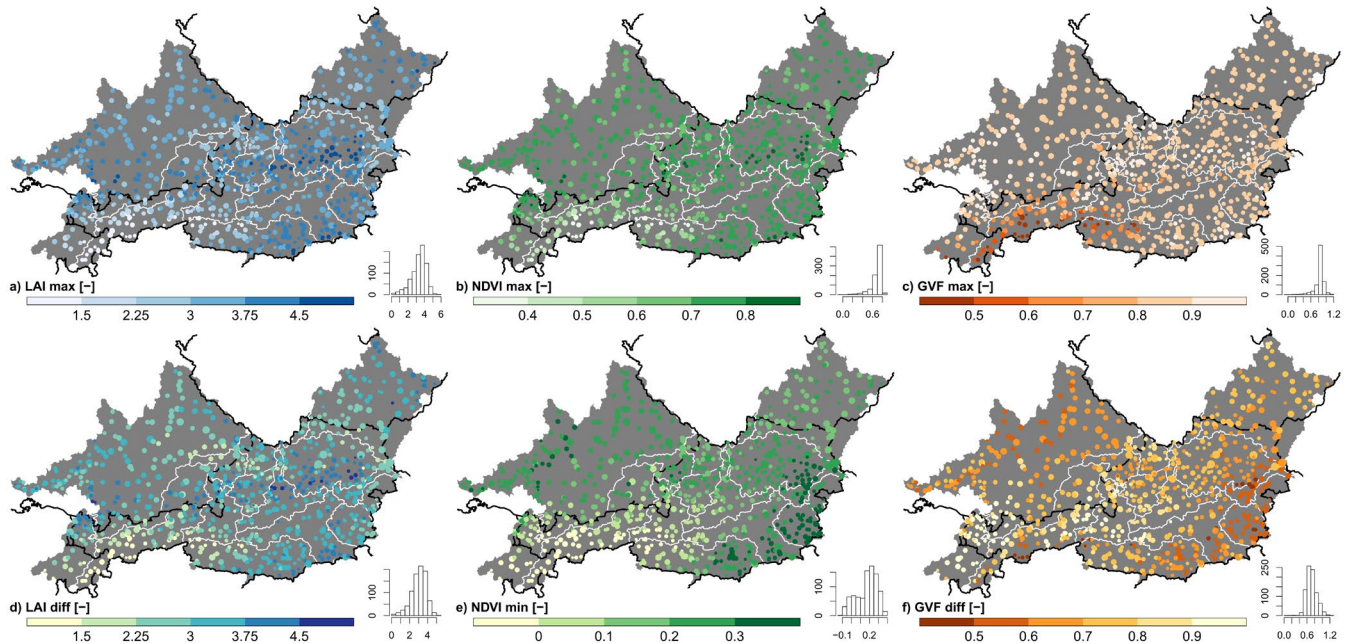
Fig. 9: Spatial distribution of vegetation indices representing the characteristics of the entire topographic catchment (basin delineation A, Fig. 2a). The histograms indicate the number of basins (out of 859) in each category. The size of the circles is proportional to the catchment area. © EuroGeographics for the administrative boundaries.

5.6 Soil characteristics

LamaH includes 10 attributes to characterize soil properties (Table A8), where 8 of them are derived from the 1 km grid sized "European Soil Database Derived Data" (ESDD; Hiederer, 2013a; 2013b). ESDD is based on the "European Soil Database" (ESD; Panagos et al., 2012; Panagos, 2006), while the maximum available soil water content (TAWC) in ESDD was calculated using pedotransfer functions (Hiederer, 2013a). ESDD provides soil attributes for a topsoil layer and a subsoil layer having the boundary at 30 cm soil depth. Values from these two layers were therefore aggregated, weighted by the available root depth ("root_dep" in Table A8), or in the case of TAWC summed up. The attribute describing the depth to bedrock "bdrk_dep" is based on the layer "average soil and sedimentary-deposit thickness" of the dataset "Global 1-km Gridded Thickness of Soil, Regolith, and Sedimentary Deposit Layers" (GGT; Pelletier et al., 2016). GGT has a spatial resolution of 30 arc seconds (approximately 1 km) and is derived from landform-specific models (for upland, lowland, slope, and valley floor) considering geomorphological principles, and incorporating data for topography, climate, and geology. Calibration and validation in GGT were performed using independent borehole profiles (Pelletier et al., 2016). The 3D Soil Hydraulic Database of Europe (3DSHD, Toth et al., 2017) dataset with a grid size of 250 m served as source for extracting the saturated hydraulic soil conductivity ("soil_condu"). 3DSHD was derived using pedotransfer functions (Toth et al., 2015) incorporating attributes from the SoilGrids250m dataset (SG250; Hengl et al., 2017), while SG250 is based on machine learning techniques including data from about 150 000 soil profiles as well as remote sensing data for climate, vegetation, geomorphology, and lithology (Hengl et al., 2017). Data within 3DSHD is provided for 7 soil layers, so a depth-weighted harmonic averaging was applied.

The provided soil attributes in LamaH may include large uncertainties and should therefore be considered with caution for several reasons. First, the soil attributes from ESD are mainly based on extrapolated observations of soil profiles and expert estimates (ESDB, 2004). Especially in the case of heterogeneous soil conditions and large distances between soil profiles the reliability of ESD dataset must be cautioned. Data from soil profiles are integrated in 3DSHD (Hengl et al., 2017; Toth et al., 2017) and the dataset of Pelletier et al. (2016) as well, but are rather used for calibration and validation. Toth et al. (2017) indicate increased unreliability for 3DSHD above 1000 m a.s.l. (about 24.2% of the project area is above 1000 m a.s.l.). Furthermore, the limitation of the soil depth at 1.5m in ESDD and 2.0 m in 3DSHD is another source of uncertainty (Boer-Euser et al., 2016). As a last point, it must be mentioned that much spatially distributed information is lost by aggregation to basin scale.

Depth to bedrock (Fig. 10a, "bedrk_dep" in Table A8) shows similar spatial patterns as mean catchment slope (Fig. 5d, R = -0.56), and mean elevation (Fig. 5b, R = -0.46). About 37 % of all 859 catchments have a mean depth to bedrock of more than 1.5 m. This depth represents the maximum root-available depth in ESDD (Fig. 10b, "root_dep"). The depth available for roots tends to be higher in Germany and the Czech Republic than in other regions. If this is an indication of different measurement methods across the countries is unclear. Low available rooting depths in Austria are, according to Fig. 10b, mainly present where the fraction of carbonate sedimentary rocks (Fig. 11c) or glaciers (Fig. 8d) is high. 40% of all catchments exhibit a mean organic soil content below 1%, while the highest organic contents are located in the southern German region (Fig. 10c,

"oc_fra"). Further interrelationships between the various grain size fractions and the dominating bedrock are recognizable: 1) A high proportion of sand (Fig. 10d, "sand_fra") is especially prevalent where the fraction of metamorphic bedrock is high (Fig. 11b, R = 0.47). 2) Moreover, the fraction of silt (Fig. 10e, "silt_fra") tends to be high on catchment level where a high fraction of carbonate sedimentary rock (Fig. 11c, R = 0.52) is present. 3) Finally, we can observe an increase in clay content (Fig. 10f, "clay_fra") with increasing proportion of mixed sedimentary rock (Fig. 11d, R = 0.47). Soil porosity (Fig. 10g, "soil_poros") shows similar spatial patterns compared to sand fraction (R = -0.79), while saturated hydraulic conductivity (Fig. 10h, "soil_condu") tends to increase with decreasing mean catchment elevation (Fig. 5b, R = -0.63). The available soil water depth (TAWC, "soil_tawc") was determined in ESDD by including water content at field capacity, gravel content and root-available depth (Hiederer, 2013a). That explains the high correlation of TAWC (Fig. 10i) with the root-available soil depth (Fig. 10b, R = 0.94).
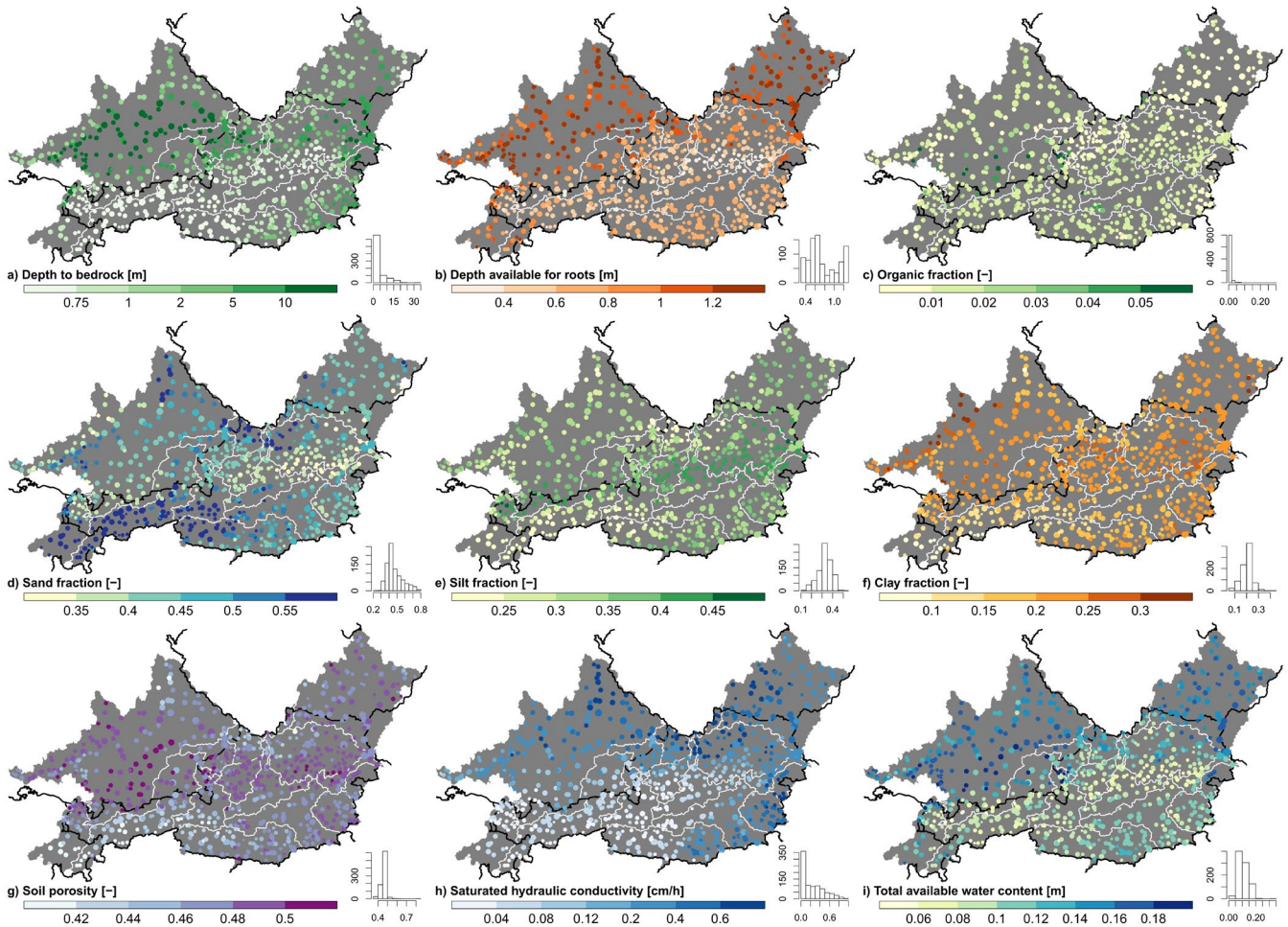
Fig. 10: Spatial distribution of soil attributes representing the characteristics of the entire topographic catchment (basin delineation A, Fig. 2a). The histograms indicate the number of basins (out of 859) in each category. The size of the circles is proportional to the catchment area. © EuroGeographics for the administrative boundaries.

5.7 Geologic characteristics

We used the datasets GLiM (Hartmann and Moosdorf, 2012; Global Lithological Map) and GLHYMPS (Gleeson et al., 2014; Global Hydrogeology Maps) for deriving 16 geologic attributes (Table A9). GLiM summarizes 92 regional geological maps in vector form and was used to extract the fractions of the different geological classes. GLiM offers 3 levels of detail, while the 1st level species the dominant lithologic class. The optional 2nd as well as 3rd level further specify, for example, the structure of the rock or local conditions (Hartmann and Moosdorf, 2012). For LamaH only the 1st level of GLiM was used, which contains 16 geological classes. The classes "evaporites", "no data" and " intermediate volcanic rocks" do not occur within the project area. The 3 most common dominant geologic classes (Fig. 11a, "gc_dom" in Table A9) across all 859 catchments are metamorphites (mt, 35.1%), carbonate sedimentary rocks (sc, 27.4%), and mixed sedimentary rocks (sm, 21.2%). Metamorphic rocks (Fig. 11b, "gc_mt_fra") are predominant along the northern border of the project area (Bohemian Massif), as well as in the more southern project area (Central Eastern Alps) and include mainly schist, gneiss and quartzite. From a hydrological point of view, the proportion of carbonate sedimentary rock is of particular interest, since a high fraction can be an indicator for karstic systems. High shares of carbonate sedimentary rocks are mainly found along the belt from the southwest to the central east of the project area (Northern Limestone Alps), the central southern border (Southern Limestone Alps) and the north-eastern border (Swabian Alb) (Fig. 11c, "gc_sc_fra"). The flysch and molasse zone (Alpine foothills and central parts of the German project area) is basically characterized by a high fraction of mixed sedimentary rocks (Fig. 11d, "gc_sm_fra"). Attributes concerning permeability and porosity of the lithologic bedrock were extracted from GLHYMPS. There is a high spatial correlation between GLHYMPS and GLiM, as geologic classes of GLiM served as a starting point for assigning hydraulic properties in GLHYMPS. Huscroft et al. (2018) declares that permeability in GLHYMPS is determined only for saturated conditions. GLHYMPS is only intended for regional-scale applications (i.e. spatial resolution greater than 5 km), as the influence of local heterogeneities such as fault zones can be neglected above this scale (Gleeson et al., 2014).

A high proportion of metamorphites or plutonites (mt, pa, pi in Fig. 11a) is commonly associated by low bedrock porosity (Fig. 11e, "geol_poros"). Catchments within the flysch and molasse zones in contrast exhibit relatively high porosity. High bedrock porosity is not necessarily followed by high subsurface permeability ("geol_perme"), yielding a much more inhomogeneous spatial pattern in Fig. 11f than in Fig. 11e. The reason may be rock structure (2nd stage of GLiM), which can have different impacts on permeability and porosity (Table 1 in Gleeson et al., 2014).
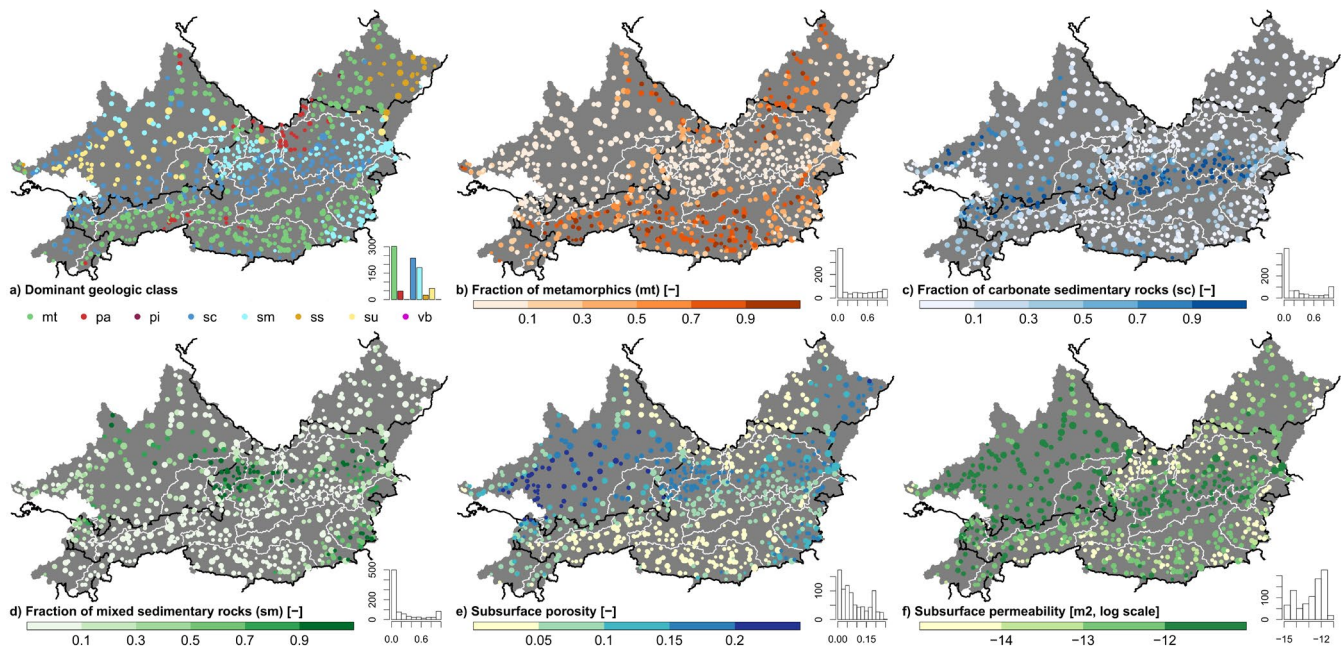
Fig. 11: Spatial distribution of geological attributes representing the characteristics of the entire topographic catchment (basin delineation A, Fig. 2a). The histograms indicate the number of basins (out of 859) in each category. The size of the circles is proportional to the catchment area. Classes in plot a): mt – Metamorphites, pa – Acid plutonic rocks, pi – Intermediate plutonic rocks, sc – Carbonate sedimentary rocks, sm – Mixed sedimentary rocks, ss – Siliciclastic sedimentary rocks, su – Unconsolidated sediments, vb – Basic volcanic rocks. © EuroGeographics for the administrative boundaries.

5.8 Information on (anthropogenic) impacts on runoff processes and measurements

We provide 4 attributes (Table 1) in order to simplify filtering and evaluation of time series of runoff gauges regarding any (anthropogenic) impact on runoff processes or its measurement. We have represented the diversity of (human) impact by 13 types of impact ("typimpact" in Table 1). The type of (human) impact on runoff or measurement was determined primarily from gauge-metadata declared by hydrographic services (BAFU, 2020; GKD, 2020; HZB, 2020; LUBW, 2020). Additionally, publicly available information, as well as manual aerial photo evaluations were used for determination. Typical types of human impact in the project area are large water reservoirs often associated with hydropower plants and cross-basin water transfers. The following types of influence were not classified because the necessary information is not consistently available, or only with great effort: 1) icing, especially at smaller rivers in winter; 2) variable channel profiles leading to inaccurate rating curves; 3) high groundwater flow in the area around the gauge; and 4) subsurface transboundary in- or outflows especially in highly karstified areas.

The hydrographs with hourly resolution in the months of January and July for the years 1990, 2005 and 2017 were additionally manually evaluated regarding systematic diurnal variations ("diur_art" / "diur_glac" in Table 1). Systematic fluctuations were further subdivided into those caused artificially (e.g. by storage power plants, power plants with swell operation or sewage treatment plants) and those caused naturally (snow or glacier melt). Summarizing the influences for every time series, the

degree of gauge impact ("degimpact") is determined mostly based on the type of impact and any systematic diurnal variations
555 (Table 2). Obviously, a gauge or catchment area can be characterized by several types of impact. In such cases, the highest
degree of impact was chosen. Geo-localization of the impacts is provided by the shapefile "Impacts.shp", which includes links
to the dam datasets GRanD ("GRAND_ID"; Lehner et al., 2011) and GOOD ("DAM_ID"; Mulligan et al., 2020) to ensure
fast access those attributes.

The spatial, as well as the frequency distribution of the degree of impact is shown in Fig. 12. 3.5% of 882 gauges are not
560 influenced (u), 48% show a low influence (l), 18.9% are moderately influenced (m) and 27% are strongly influenced (s), while
2.6% belong to class (x). Low influenced gauges are predominant in the northwest of the German project area, in the north of
the Austrian central region (river region 5, 6, 7, 8, 9, 10 in Fig. 1), in the east (river region 16), as well as in the south of Austria
(east of river region 18). Strongly influenced gauges are in contrast mainly prevalent, where large water reservoirs are in
operation for hydropower generation (primarily in the Alpine region) and for seasonal water balancing or flood protection
565 (primarily in the Czech Republic and in the north of the German project area). It should be noted that gauges located far
downstream of large reservoirs may still be strongly influenced by them.
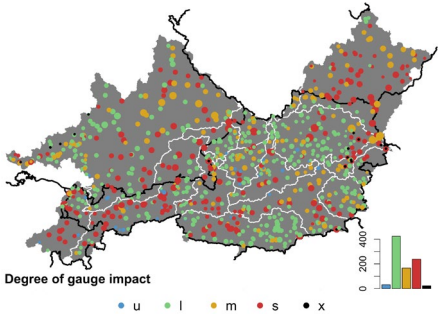
Fig. 12: Degree of (anthropogenic) impact on gauges / catchments. The histogram indicates the number of gauges (out of 882) in each category. The size of the circles is proportional to the catchment area. Classes: u – no influence, l – low influence, m – moderate
570 **influence, s – strong influence, x – not considered in basin delineation. © EuroGeographics for the administrative boundaries.**

Table 1: Attributes for (anthropogenic) gauge and catchment interference.

Attribute	Description	Data source
typimpact	Type of gauge impact, categorized in 13 classes: A – water reservoir with all-season water filling B – flood retention reservoir C – lake with controllable outlet (e.g. weir) D – lake with unaffected outlet E – water withdrawals F – emergency outlet of water reservoir G – extreme events are influenced / not properly measured H – artificial channel	BAFU (2020), CHMI (2020), GKD (2020), HZB (2020), LUBW (2020)

	I – water intake (from neighbouring river or catchment)	
	J – weed / vegetation near gauge	
	K – fishing ponds	
	L – high infiltration	
	M – (karstic-) spring	
diur_art	Unnatural systematic variations in hydrograph with hourly resolution, binary classification (0 - no, 1 - yes)	see above
diur_glac	Systematic fluctuations in the hydrograph with hourly resolution, which are caused by glacier melt, binary classification (0 - no, 1 - yes)	see above
degimpact	Degree of gauge impact, classes see Table 2.	see above

Table 2: Criteria for the different degrees of gauge impact.

degimpact	Criteria
u – no influence	If there is no obvious type of impact ("typimpact" in Table 1) and the gauge is located above populated areas. Artificial change of catchment size is less than 1% in case of impact type E (water withdrawals) or I (water intake) [a].
l – low influence	Gauges located in or downstream of urban areas and without any type of impact (potential influence by undetected water withdrawals or stormwater drains) or type of impact is declared with D (lake with unaffected outlet) or J (weed / vegetation in gauge proximity). Artificial change of catchment size lies between 1 and 3% in case of impact type E or I [a].
m – moderate influence	Type of impact is attributed with B (flood retention reservoir), C (lake with controllable outlet), F (emergency outlet of water reservoir), G (extreme events are influenced / not properly measured), K (fishing ponds) or L (high infiltration). An exception was made for 3 gauges in the upper Danube, which can be strongly (s) affected by full seepage during the summer months (Hötzl, 1996). Artificial change of catchment size is between 3 and 10% in case of impact type E or I [a].
s – strong influence	Gauges with impact type A (water reservoir with all-season water filling) were assigned a strong (s) degree of impact in most cases. An exception was made in case of very large catchment areas (moderate degree of impact for selected Danube gauges). Artificial change of catchment size is more than 10% in case of impact type E or I [a]. Systematic diurnal variations of artificial origin ("diur_art" in Table 1).
x – not considered	Gauges, which 1) do not have a clearly assignable catchment area (e.g. gauges at artificial channels (impact type H) or below karstic springs), 2) are characterised by several time series (e.g. with or without consideration of mill channels; in this case it is possible that there are two gauges per point, one declared with "degimpact" = x and one with another degree of impact), and 3) have too many gaps (> 50%) in the

	time series. These gauges were subsequently assigned no meteorological time series or catchment attributes due to lack of basin delineation.

[a] The hydrographic yearbook of Austria declares anthropogenic cross-basin water transfers by increasing or decreasing the natural catchment area of a gauge (BMLFUW, 2013). There is no information regarding artificial changes in catchment size for gauges outside Austria. Here, the degree of impact was additionally determined, and also at Austrian gauges influenced by other kinds of water withdrawal (river branches, diversions or irrigation), on the basis of publicly available information, as well as aerial photo analyses. We thereby mostly assigned a strong degree of impact (s), but in a few cases (e.g. withdrawals for drinking water) also a moderate degree (m).

6 Hydrological model

6.1 Model setup

Finally, we set up a conceptual hydrological model in order to check the inputs for plausibility and to be able to provide a baseline / benchmark model for further research. We applied the COSERO (COntinuous SEmi-distributed RunOff) model, which is a conceptual, semi-distributed hydrological model. It has a quite similar model structure as the well-known HBV model (Bergström, 1992). COSERO was developed in the 1990s at the University of Natural Resources and Life Sciences, Vienna, initially for runoff forecasting in alpine catchments in Austria (Nachtnebel et al., 1993). The model was also used in various hydrological studies in Austria (e.g. Nachtnebel and Fuchs, 2004; Eder et al., 2005; Kling and Nachtnebel, 2009a/b; Stanzel and Nachtnebel, 2010; Herrnegger et al., 2012, Kling et al., 2012, Frey and Holzmann, 2015; Herrnegger et al., 2015; Herrnegger et al., 2018; Klingler et al., 2020; Wesemann et al., 2018) and serves as a core for several operational discharge forecasting systems in Austria (e.g. Stanzel et al., 2008; Schulz et al., 2016; Wesemann et al., 2018). The performance of COSERO has been evaluated so far in different climates as well as in different spatiotemporal resolutions (e.g. Enzinger, 2009; Kling et al., 2015; Mehdi et al., 2021). COSERO incorporates interception, soil water storage, snow accumulation and melting (modified temperature-index approach, including log-normal distribution of snow-depth, cold-content of snow-pack, water holding capacity of snow-pack, refreezing of retained melt-water, settlement of snow-pack; see Frey and Holzmann, 2015), glacier melting, actual evapotranspiration (function of PET, snow sublimation, soil moisture and interception losses), division of runoff generation into different components (surface flow, interflow and baseflow), and routing through a cascade of (non-) linear reservoirs. Required inputs are time series for precipitation, air temperature and optionally PET as well as a parameter field including topology (Kling et al., 2015). Time series for PET can be derived model internally from the air temperature using the Thornthwaite approach (Thornthwaite and Mather, 1957).

Here, COSERO is applied with a lumped spatial discretization based on intermediate catchments (basin delineation B) and daily resolution. PET time series are derived internally following the Thornthwaite approach, since the PET time series from ERA5-Land are not included in LamaH (section 4.2). These derived PET time series are provided in addition to numerous other modelled fluxes within LamaH (Table C2). Artificial water reservoirs are not considered in COSERO. In contrast, cross-

basin water transfers using information from LamaH (see Table A11; "Crossbasin_water_transfers.csv"; "Impacts.shp") and glaciers (if more than 10% area fraction) are accounted for. Calibration of 20 parameters (Table C1) was performed using the DDS algorithm (Tolson and Shoemaker, 2007) with a single-objective function (NSE, 100%) and 1 000 DDS iterations for the period 1 January 1982 to 30 September 2000. The year 1981 was used as a spin-up phase to enable system states to consolidate and reach an equilibrium. A (intermediate) basin was calibrated in an individual run, if the associated runoff gauge has observations at least since 1999. Otherwise (flag "fewobs" in supplementary text- and shapefiles is set to "1"), this basin was treated as unobserved and calibrated together with the next downstream intermediate catchment, whose associated gauge has sufficiently long records. The results of those basins with no or to less runoff recordings in calibration phase are not evaluated (54 basins) and the runoff simulations are set to "-999" in the provided runoff simulations (Table C2). The period from 1 October 2000 to 30 September 2017 was used as validation phase.

6.2 Model results

We evaluate the model results using standard performance metrics NSE (Eq. 2; Gupta and Kling, 2011; Jain and Sudheer, 2008; Knoben et al., 2019; McCuen et al., 2006; Nash and Sutcliffe, 1970; Schaefli and Gupta, 2007) and percentual (p) long-term BIAS (Eq. 3).

$$NSE = 1 - \frac{\sum_t^n (Q_{sim,t} - Q_{obs,t})^2}{\sum_t^n (Q_{obs,t} - \overline{Q_{obs}})^2} \tag{2}$$

$$pBIAS = \frac{\overline{Q_{sim}} - \overline{Q_{obs}}}{\overline{Q_{obs}}} \times 100 \tag{3}$$

where Q_{sim} represents the simulated and Q_{obs} the observed runoff. The dash above the variable indicates the arithmetic mean. The NSE ranges from -9.26 (calibration) / -13.96 (validation) to 0.91 / 0.90 (Fig. 13b) with an area-unweighted median of 0.64 / 0.60. Inadequate model performance (Fig. 13a) can mostly be explained by: (i) cross-basin water transfers in karstified regions (see Fig. 11c), which is not accounted for in the model, (ii) a clear water surplus especially in eastern regions caused by overestimation in precipitation inputs or underestimation in evapotranspiration (Fig. 13c) or (iii) artificial structures, which were completed after the start of the calibration period (and thus were not specified in the artificial cross-basin water transfers). Rather good NSE values (> 0.6) can be observed primarily at: (i) gauges with large catchment area (Fig. 13a), (ii) rainfall-dominated catchments (Fig. 6c) or (iii) gauges, which are not too strongly influenced by large water reservoirs.

The overall area-unweighted median pBIAS (Fig. 13c) is +6.1% in calibration and +4.4% in validation phase, which indicates either a precipitation surplus provided by ERA5-Land or underestimation of evapotranspiration. Herrnegger et al. (2012) show that the Thornthwaite approach tends to provide too low PET sums in alpine regions. Although air temperature is an important driver or proxy for evapotranspiration, other meteorological parameters, namely radiation, wind and relative humidity, are equally or probably more important factors. This is especially the case, where lower air temperatures are present (especially in alpine regions) and other meteorological drivers for evapotranspiration, apart from temperature, become more important. The area-weighted mean of the PET-correction factor "ETSLPCOR" after calibration is 1.73 (with an upper boundary of 2.0,

see Table C1), which indicates a compensation of too low PET values in the calibration procedure. Considering that the long-term evapotranspiration totals of the model output ("ETAsum" in the supplied shapefile "Hyd_model.shp") seems quite plausible (e.g. compared to Fig. 20 in Herrnegger et al., 2012 or Map 3.3 in HAO, 2007), the reason for runoff surplus is likely a precipitation surplus in the ERA5-Land input. Klingler et al. (2020) show that CHIRPS Daily v2 (Funk et al., 2015) reflects long-term precipitation sums in the Mur catchment in the south of the Alps quite well. Fig. 4e in contrast indicates that ERA5-Land in general provides considerably higher precipitation sums compared to CHIRPS Daily v2. This, in combination with our restriction to simulate somewhat realistic ETA-fluxes, probably explains the many positive biases in the simulations of alpine catchments. The tight corset regarding ETA-fluxes, in combination with too high precipitation input, clearly leads to a lower model performance. Machine Learning approaches, with few exceptions (e.g. Hoedt et al., 2021), ignore these physical constraints and it is clear that higher model performance can be achieved, when ignoring the mass-balance or the realistic partitioning of precipitation in ETA and runoff.

Fig. 13: Plot a) Spatial distribution of NSE in validation phase. Plot b) Cumulative distribution of NSE in calibration and validation phase. Plot c) Spatial distribution of percent bias in validation phase (positive values indicate a simulated surplus). The size of the circles in plot a) and c) is proportional to the catchment area. © EuroGeographics for the administrative boundaries.

Lastly, providing something like a disclaimer, it is important to stress that the simulation results stem from a large-scale model, which in this form has previously not been available. To our knowledge, no hydrological model existed, which (i) covers such a large domain in Central Europe in such detail (~170 000 km² in 9 countries divided in 859 sub-basins), (ii) uses so many discharge observations for calibration and validation, and (iii) which considers cross-basin water transfers. Although great care and love for detail was invested in the model setup of COSERO, it cannot be guaranteed that all local hydrometeorological features are represented and room for improvement probably remains. Consequently, this baseline model may locally exhibit significant deviations from real-world hydrologic conditions. This however generally remains a challenge for many large-scale hydrological models.

7 Summary and conclusions

Hydrological studies often require an extensive foundation of data. In large-scale or cross-national projects, it is therefore often laborious and time-consuming to collect the required data and then to homogenize the usually different formats, definitions

and conventions. Reasons are for instance the different organizational forms of the hydrographic authorities or communication barriers. LamaH provides a unique, homogeneous data base for hydrological and other environmental sciences, that can overcome the mentioned barriers. Apart from the complete territory of Austria, LamaH includes all neighboring upstream areas of the rivers flowing through Austria as well. LamaH contains runoff time series as well as 15 meteorological time series (daily and hourly resolution) and over 60 attributes for 859 catchments. Additionally, simulations from a conceptual hydrological model provides a baseline for further investigations. Three basin delineations allow investigations with individual catchments (as known from CAMELS) as well as within an interconnected river network considering intermediate catchments. It is clear that LamaH contains deficits and uncertainties due to the large number of data sources included. We however tried to consider and discuss most of these limitations.

Blöschl et al. (2019b) highlighted numerous open hydrological challenges, such as runoff prediction in ungauged basins (PUB). Methods based on machine learning show promising results for time series prediction (e.g. Kratzert et al., 2019a; 2019b; Kratzert et al., 2018). However, uniformly structured "large-sample" datasets are helpful when applying these data-driven methods, because on the one hand the necessary preparatory work is drastically reduced and on the other hand the exchange or comparability of the modelling results is considerably facilitated. Given the scope of LamaH, we hope that this dataset will serve as a solid data base for further investigations in various fields of hydrology and adjacent fields of environmental science. The high variability in the data in combination with the interconnected river network as well as the high temporal resolution of the time series could grant an improved understanding of processes in water transfer and storage, if appropriate methods are used.

Data availability. LamaH is freely available at https://doi.org/10.5281/zenodo.4525244 (Klingler et al., 2021). The dataset is basically divided into 7 parts including basin delineation A/B/C, gauges, stream network, hydrological model and appendix. The first 4 parts mentioned contain shapefiles, various text files regarding the attributes as well as time series. The stream network is available with shapefiles, which contain numerous attributes. Various in- and outputs (e.g. parameter field, fluxes or evaluations) are provided for the hydrologic model. The entire folder structure, supplementary information regarding the time series, and required references are in the folder "Info". The runoff time series of the German federal states Bavaria and Baden-Württemberg are retrospective checked and updated by the hydrographic services. Therefore, it might be appropriate to obtain more up-to-date runoff data from GKD (2020) or LUBW (2020). Please consider also the disclaimer stated at Zenodo.

Code availability. We have used R-Codes from Nans Addor (Addor, 2017b) for reproducing the climatic (Table A4) and hydrological (Table A5) indices as well as for creating the Figures 3, 5 to 13a/c. The color schemes in the plots are often based on ColorBrewer 2.0 (Brewer, 2021). Further relevant R- and Python-scripts for reproducing the dataset are available in the folder "G_appendix".

Required additional references when using LamaH. We ask kindly for compliance, as the agreement to citation was usually the claim for sharing the data. BAFU, 2020; CHMI, 2020; GKD, 2020; HZB, 2020; LUBW, 2020**;** BMLFUW, 2013; Broxton et al., 2014; CORINE, 2012; EEA, 2019; ESDB, 2004; Farr et al., 2007; Friedl and Sulla-Menashe, 2019; Gleeson et al., 2014;

HAO, 2007; Hartmann and Moosdorf, 2012; Hiederer, 2013a; Hiederer, 2013b; Linke et al., 2019; Muñoz Sabater et al., 2021; Muñoz Sabater, 2019a; Myneni et al., 2015; Pelletier et al., 2016; Toth et al., 2017; Trabucco and Zomer, 2019; Vermote 2015.

695 **Author contributions.** CK, KS, MH initiated the investigation and designed the study. CK requested the data base, processed the time series and computed the various attributes. The hydrological baseline model was set up by CK and MH while the manuscript was prepared by CK with contributions from all co-authors.

Competing interests. The authors declare that they have no conflict of interest.

Financial support. This work was in parts funded by the Austrian Science Fund FWF, project number P 31213.

700 **Acknowledgements.** We would like to thank the hydrographic offices from the (federal) states Austria, Baden-Württemberg, Bayern, Czech Republic and Switzerland for providing the runoff time series. Data processing was performed using the freely available software packages R (R Core Team, 2020), Python (Python Software Foundation, 2020), and QGIS (QGIS Development Team, 2020). Special thanks to all who have developed the numerous open source software, packages and extensions or who share their experiences in the numerous online forums. LamaH would not have been possible without the

705 institutions, working groups and individuals who worked, in some cases for several years, on the used open-source datasets.

Review statement. We would like to acknowledge the valuable inputs from the two reviewers Gemma Coxon and Mathis Messager. Their accurate and comprehensive reviews helped to significantly improve the paper and the dataset. Gratitude is also paid to the editor Lukas Gudmundsson as well as Daniel Klotz, who suggested to implement a hydrological baseline model. Lastly, we would like to thank Frederik Kratzert, who did a lot of testing and contributed some proposals for improving

710 the structure of LamaH.

References

Addor, N., Do, H. X., Alvarez-Garreton, C., Coxon, G., Fowler, K., and Mendoza, P. A.: Large-sample hydrology: recent progress, guidelines for new datasets and grand challenges, Hydrolog. Sci. J., 1–14, https://doi.org/10.1080/02626667.2019.1683182, 2019.

715 Addor, N., Newman, A. J., Mizukami, N., and Clark, M.: The CAMELS data set: catchment attributes and meteorology for large-sample studies, Hydrol. Earth Syst. Sci., 21, 5293–5313, https://doi.org/10.5194/hess-21-5293-2017, 2017a.

Addor, N.: R scripts for reproducing the climatic and hydrological indices, as well as for creating the maps, GitHub, available at: https://github.com/naddor/camels (last access: 02.03.2020), 2017b.

Allen, R. G., Pereira, L. S., Raes, D., and Smith, M.: Crop Evapotranspiration. Guidelines for Computing Crop Water
720 Requirements, FAO Irrigation and Drainage Paper 56, Food and Agriculture Organization (FAO) of the United Nations, Rome, ISBN 92-5-104219-5, 300pp, 1998.

Alvarez-Garreton, C., Mendoza, P. A., Boisier, J. P., Addor, N., Galleguillos, M., Zambrano-Bigiarini, M., Lara, A., Puelma, C., Cortes, G., Garreaud, R., McPhee, J., and Ayala, A.: The CAMELS-CL dataset: catchment attributes and

meteorology for large sample studies – Chile dataset, Hydrol. Earth Syst. Sci., 22, 5817–5846,
725   https://doi.org/10.5194/hess-22-5817-2018, 2018.

Arora, V. K.: The use of the aridity index to assess climate change effect on annual runoff, Journal of Hydrol., 265, 164–177,
https://doi.org/10.1016/S0022-1694(02)00101-4, 2002.

BAFU: Federal Office for the Environment – Hydrology Division, Bern, Switzerland (runoff data received: 23.09.2020),
2020.

730   Beck, H. E., Wood, E. F., Pan, M., Fisher, C. K., Miralles, D. G., van Dijk, A. I. J. M., McVicar, T. R., and Adler, R. F.:
MSWEP V2 Global 3-Hourly 0.1 Precipitation: Methodology and Quantitative Assessment, B. Am. Meteorol. Soc.,
100(3), 473–500, https://doi.org/10.1175/BAMS-D-17-0138.1, 2019.

Beck, H. E., Vergopolan, N., Pan, M., Levizzani, V., van Dijk, A. I. J. M., Weedon, G. P., Brocca, L., Pappenberger, F.,
Huffman, G. J., and Wood, E. F.: Global-scale evaluation of 22 precipitation datasets using gauge observations and
735   hydrological modeling, Hydrol. Earth Syst. Sci., 21, 6201–6217, https://doi.org/10.5194/hess-21-6201-2017, 2017.

Beck, H. E., Van Dijk, A. I. J. M., Miralles, D. G., De Jeu, R. A. M., Bruijnzeel, L. A., McVicar, T. R., and Schellekens, J.:
Global patterns in base flow index and recession based on streamflow observations from 3394 catchments, Water
Resour. Res., 49, 7843–7863, https://doi.org/10.1002/2013WR013918, 2013.

Berghuijs, W. R., Sivapalan, M., Woods, R. A., and Savenije, H. H. G.: Patterns of similarity of seasonal water balances: A
740   window into streamflow variability over a range of time scales, Water Resour. Res., 50, 5638–5661,
https://doi.org/10.1002/2014WR015692, 2014.

Bergström, S.: The HBV model - its structure and applications, SMHI Reports Hydrology, No 4, ISSN 0283-1104, 32pp,
1992.

Blöschl, G., Hall, J., Viglione, A., Perdigão, R. A. P., Parajka, J., et al.: Changing climate both increases and decreases
745   European river floods, Nature, 573, 108–111, https://doi.org/10.1038/s41586-019-1495-6, 2019a.

Blöschl, G., Bierkens, M. F. P., Chambel, A., Cudennec, C., Destouni, G., et al.: Twenty-three unsolved problems in
hydrology (UPH) – a community perspective, Hydrolog. Sci. J., 64, 1141–1158,
https://doi.org/10.1080/02626667.2019.1620507, 2019b.

Blöschl, G., Sivapalan, M., Savenije, H., Wagener, T., and Viglione, A. (Eds.): Runoff prediction in ungauged basins:
750   synthesis across processes, places and scales, Cambridge University Press, Cambridge, ISBN 9781107028180, 490pp,
2013.

BMLFUW: Hydrographic Yearbook of Austria 2013, Federal Ministry of Agriculture, Regions and Tourism – Hydrographic
Central Office, Vienna, Austria, available at: https://www.bmlrt.gv.at/dam/jcr:bb100102-eac3-4b51-8d8d-
f40b94e5d546/Jahrbuch_2013_Datenteil.pdf (last access: 16.12.2020), 2013.

755   Boer-Euser, T., McMillan, H. K., Hrachowitz, M., Winsemius, H. C., and Savenije, H. H. G.: Influence of soil and climate
on root zone storage capacity, Water Resour. Res., 52, 2009–2024, https://doi.org/10.1002/2015WR018115, 2016.

Bossard, M., Feranec, J., and Otahel, J.: CORINE land cover technical guide – Addendum 2000, Technical report No 40, European Environment Agency, Copenhagen, Denmark, 105pp, 2000.

Brewer, C. A.: ColorBrewer 2.0, available from: http://colorbrewer2.org/ (last access: 27.05.2021), 2021.

760 Broxton, P. D., Zeng, X., Scheftic, W., and Troch P. A.: A MODIS-Based Global 1-km Maximum Green Vegetation Fraction Dataset, Journal of applied Meteorology and Climatology, 53, 1996–2004, https://doi.org/10.1175/JAMC-D-13-0356.1, 2014.

Budyko, M. I.: Climate and Life; Academic Press: New York, NY, USA, 1974.

Büttner, G. and Maucha, G.: The thematic accuracy of Corine land cover 2000 – Assessment using LUCAS (land use/cover
765 area frame statistical survey), Technical report No 7/2006, European Environment Agency, Copenhagen, Denmark, ISBN 92-9167-844-9, 90pp, 2006.

Chagas, V. B. P., Chaffe, P. L. B., Addor, N., Fan, F. M., Fleischmann A. S., Paiva, R. C. D, and Siqueira V. A.: CAMELS-BR: hydrometeorological time series and landscape attributes for 897 catchments in Brazil, Earth Syst. Sci. Data, 12, 2075–2096, https://doi.org/10.5194/essd-12-2075-2020, 2020.

770 Chapman, T: A comparison of algorithms for stream flow recession and baseflow separation, Hydrol. Processes, 13(5), 701–714, https://doi.org/10.1002/(SICI)1099-1085(19990415)13:5<701::AID-HYP774>3.0.CO;2-2, 1999.

CHMI: Czech Hydrometeorological Institute, Brno, Czech Republic (runoff data received: 14.12.2020), 2020.

Clausen, B. and Biggs, B. J. F.: Flow variables for ecological studies in temperate streams: groupings based on covariance, J. Hydrol., 237, 184–197, https://doi.org/10.1016/S0022-1694(00)00306-1, 2000.

775 COPa: European Space Agency & European Commission, Copernicus Program, Copernicus Open Access Hub, available at: https://scihub.copernicus.eu/ (last access: 22.02.2021), 2021.

COPb: European Space Agency & European Commission, Copernicus Program, Copernicus Climate Data Store, available at: https://cds.climate.copernicus.eu/#!/home (last access: 22.02.2021), 2021.

CORINE: CORINE Land Cover 2012, European Environment Agency, Copenhagen, Denmark, available at:
780 https://land.copernicus.eu/pan-european/corine-land-cover (last access: 02.03.2020), 2012.

Court, A.: Measures of streamflow timing, J. Geophys. Res., 67, 4335–4339, https://doi.org/10.1029/JZ067i011p04335, 1962.

Coxon, G., Addor, N., Bloomfield, J. P., Freer, J., Fry, M., Hannaford, J., Howden, N. J. K., Lane, R., Lewis, M., Robinson, E. L., Wagener, T., and Woods, R.: CAMELS-GB: Hydrometeorological time series and landscape attributes for 671
785 catchments in Great Britain, Earth Syst. Sci. Data, 12, 2459–2483, https://doi.org/10.5194/essd-12-2459-2020, 2020.

Do, H. X., Gudmundsson, L., Leonard, M., and Westra, S.: The Global Streamflow Indices and Metadata Archive (GSIM) – Part 1: The production of a daily streamflow archive and metadata, Earth Syst. Sci. Data, 10, 765–785, https://doi.org/10.5194/essd-10-765-2018, 2018.

Döll, P., Douville, H., Güntner, A., Schmied, H. M., and Wada, Y.: Modelling freshwater resources at the global scale:
790 challenges and prospects, Surv. Geophys., 37, 195–221, https://doi.org/10.1007/s10712-015-9343-1, 2016.

Duan, Q., Schaake, J., Andréassian, V., Franks, S., Goteti, G., Gupta, H. V., Gusev, Y. M., Habets, F., Hall, A., Hay, L., Hogue, T., Huang, M., Leavesley, G., Liang, X., Nasonova, O. N., Noilhan, J., Oudin, L., Sorooshian, S., Wagener, T., and Wood, E. F.: Model Parameter Estimation Experiment (MOPEX): An overview of science strategy and major results from the second and third workshops, Journal of Hydrology, 320, 3–17, https://doi.org/10.1016/j.jhydrol.2005.07.031, 2006.

Eckhardt, K.: A comparison of baseflow indices, which were calculated with seven different baseflow separation methods, J. of Hydrol., 352, 168–173, https://doi.org/10.1016/j.jhydrol.2008.01.005, 2008.

Eder, G., Fuchs, M., Nachtnebel, H. P., and Loibl, W.: Semidistributed modelling of the monthly water balance in an alpine catchment, Hydrological Processes, 19, 2339–2360, https://doi.org/10.1002/hyp.5888, 2005.

EEA: EU-Hydro – River Network Database, Version 1.2, European Environment Agency under the framework of the Copernicus program, available at: https://land.copernicus.eu/imagery-in-situ/eu-hydro/eu-hydro-river-network-database (last access: 22.10.2020), 2019.

Enzinger, P. A.: Modelling the hydrological cycle in a Siberian catchment: application of the COSERO model, Master thesis, Institute for Water Management, Hydrology and Hydraulic Engineering, University of Natural Resources and Life Science, Vienna, Austria, https://zidapps.boku.ac.at/abstracts/download.php?dataset_id=7172&property_id=107, 142pp, 2009.

ESDB: The European Soil Database distribution version 2.0, European Commission and the European Soil Bureau Network, CD-ROM, EUR 19945 EN, 2004.

Falkenmark, M. and Chapman, T.: Comparative hydrology: An ecological approach to land and water resources Unesco, UNESCO, Paris, 1989.

Fan, Y., Clark, M., Lawrence, D. M., Swenson, S., Band, L. E., Brantley, S. L., Brooks, P. D., Dietrich, W. E., Flores, A., Grant, G., Kirchner, J. W., Mackay, D. S., McDonnell, J. J., Milly, P. C. D., Sullivan, P. L., Tague, C., Ajami, H., Chaney, N., Hartmann, A., Hazenberg, P., McNamara, J., Pelletier, J., Perket, J., Rouholahnejad-Freund, E., Wagener, T., Zeng, X., Beighley, E., Buzan, J., Huang, M., Livneh, B., Mohanty, B. P., Nijssen, B., Safeeq, M., Shen, C., Verseveld, W., Volk, J., and Yamazaki, D.: Hillslope Hydrology in Global Change Research and Earth System Modeling, Water Resour. Res., 55, 1737–1772, https://doi.org/10.1029/2018WR023903, 2019.

Fan, Y.: Groundwater in the Earth's critical zone: Relevance to large-scale patterns and processes: Groundwater at large scales, Water Resour. Res., 51, 3052–3069, https://doi.org/10.1002/2015WR017037, 2015.

Farr, T. G., Rosen, P. A., Caro, E., Crippen, R., Duren, R., Hensley, S., Kobrick, M., Paller, M., Rodriguez, E., Roth, L., Seal, D., Shaffer, S., Shimada, J., Umland, J., Werner, M., Oskin, M., Burbank, D., and Alsdorf, D. E.: The shuttle radar topography mission: Reviews of Geophysics, 45(2), RG2004, available at: https://doi.org/10.1029/2005RG000183, 2007.

Frey, S. and Holzmann, H.: A conceptual, distributed snow redistribution model, Hydrol. Earth Syst. Sci., 19, 4517–4530, https://doi.org/10.5194/hess-19-4517-2015, 2015.

825 Friedl, M. and Sulla-Menashe, D.: MCD12Q1 MODIS/Terra+Aqua Land Cover Type Yearly L3 Global 500m SIN Grid V006 [Data set], NASA EOSDIS Land Processes DAAC, available at: https://doi.org/10.5067/MODIS/MCD12Q1.006 (last access: 12.03.2020), 2019.

Funk, C., Peterson, P., Landsfeld, M., Pedreros, D., Verdin, J., Shukla, S., Husak, G., Rowland, J., Harrison, L., Hoell, A., and Michaelsen, J.: The climate hazards infrared precipitation with stations-a new environmental record for

830 monitoring extremes, Scientific Data, 2, Article Number: 150066 (2015), https://doi.org/10.1038/sdata.2015.66, 2015.

GEEa; Google Earth Engine Platform, available at: https://earthengine.google.com/platform/ (last access: 22.02.2021), 2021.

GEEb: Google Earth Engine Data Catalog, available at: https://developers.google.com/earth-engine/datasets (last access: 22.01.2021), 2021.

Ghiggi, G., Humphrey, V., Seneviratne, S. I., and Gudmundsson, L.: GRUN: an observation-based global gridded runoff

835 dataset from 1902 to 2014, Earth Syst. Sci. Data, 11, 1655–1674, https://doi.org/10.5194/essd-11-1655-2019, 2019.

GKD: Bavarian State Office for the Environment – Hydrographic Service, Munich, Germany, available at: https://www.gkd.bayern.de/en/rivers/discharge/tables (runoff data downloaded: 15.09.2020), 2020.

Gleeson, T., Moosdorf, N., Hartmann, J., and van Beek, L. P. H.: A glimpse beneath earth's surface: GLobal HYdrogeology MaPS (GLHYMPS) of permeability and porosity, Geophys. Res. Lett., 41, 3891–3898,

840 https://doi.org/10.1002/2014GL059856, available at: https://dataverse.scholarsportal.info/dataset.xhtml?persistentId=doi:10.5683/SP2/DLGXYO (last access: 12.03.2020), 2014.

Gorelick, N., Hancher, M., Dixon, M., Ilyushchenko, S., Thau, D., and Moore, R.: Google Earth Engine: Planetary-scale geospatial analysis for everyone, Remote Sensing of Environment, 202, 18–27,

845 https://doi.org/10.1016/j.rse.2017.06.031, 2017.

Gudmundsson, L., Leonard, M., Do, H. X., Westra, S., and Seneviratne, S. I.: Observed Trends in Global Indicators of Mean and Extreme Streamflow, Geophys. Res. Lett., 46, 756–766, https://doi.org/10.1029/2018GL079725, 2019.

Gudmundsson, L., Do, H. X., Leonard, M., and Westra, S.: The Global Streamflow Indices and Metadata Archive (GSIM) – Part 2: Quality control, time-series indices and homogeneity assessment, Earth Syst. Sci. Data, 10, 787–804,

850 https://doi.org/10.5194/essd-10-787-2018, 2018.

Gupta, H. V., Perrin, C., Blöschl, G., Montanari, A., Kumar, R., Clark, M., and Andréassian, V.: Large-sample hydrology: a need to balance depth with breadth, Hydrol. Earth Syst. Sci., 18, 463–477, https://doi.org/10.5194/hess-18-463-2014, 2014.

Gupta, H. V. and Kling, H.: On typical range, sensitivity, and normalization of Mean Squared Error and Nash-Sutcliffe

855 Efficiency type metrics, Water Resour. Res., 47, W10601, https://doi.org/10.1029/2011WR010962, 2011.

HAO: Hydrological Atlas of Austria (digHAO), 3. Delivery, Federal Ministry of Agriculture, Regions and Tourism – Hydrographic Central Office, Vienna, Austria, ISBN 3-85437-250-7, 2007.

Hargreaves, G. H.: Defining and Using Reference Evapotranspiration, Journal of Irrigation and Drainage Engineering, 120(6), 1132–1139, https://doi.org/10.1061/(ASCE)0733-9437(1994)120:6(1132), 1994.

860 Hartmann, J. and Moosdorf, N.: The new global lithological map database GLiM: A representation of rock properties at the Earth surface, Geochem. Geophy. Geosy., 13, 1–37, https://doi.org/10.1029/2012GC004370, 2012.

Hengl, T., Mendes de Jesus, J., Heuvelink, G. B. M., Ruiperez Gonzalez, M., Kilibarda, M., et al.: SoilGrids250m: Global gridded soil information based on machine learning, edited by: Bond-Lamberty, B., PLoS ONE, 12, e0169748, https://doi.org/10.1371/journal.pone.0169748, 2017.

865 Hennermann, K. and Guillory, A.: ERA5: uncertainty estimation, CDS dataset documentation, European Centre for Medium-Range Weather Forecasts (ECMWF), available at: https://confluence.ecmwf.int/display/CKB/ERA5%3A+uncertainty+estimation (last access: 30.11.2020), 2020.

Herrnegger, M., Senoner, T., and Nachtnebel, H. P.: Adjustment of spatio-temporal precipitation patterns in a high Alpine environment, J. Hydrol., 556, 913–921, https://doi.org/10.1016/j.jhydrol.2016.04.068, 2018.

870 Herrnegger, M., Nachtnebel, H. P., and Schulz, K. (2015): From runoff to rainfall: inverse rainfall–runoff modelling in a high temporal resolution, Hydrology and Earth System Science, 19, 4619–4639, https://doi.org/10.5194/hess-19-4619-2015, 2015.

Herrnegger, M., Nachtnebel, H. P., and Haiden, T.: Evapotranspiration in high alpine catchments – an important part of the water balance!, Hydrol. Res., 43(4), 460–475, https://doi.org/10.2166/nh.2012.132, 2012.

875 Hersbach, H., Bell, B., Berrisford, P., Hirahara, S., Horányi, A., Muñoz-Sabater, J., et al.: The ERA5 global reanalysis, Quarterly Journal of the Royal Meteorol. Soc., 146(730), 1999–2049, https://doi.org/10.1002/qj.3803, 2020.

Hiederer, R.: Mapping Soil Properties for Europe - Spatial Representation of Soil Database Attributes, Luxembourg: Publications Office of the European Union, 47pp, EUR26082EN Scientific and Technical Research series, ISSN 1831- 9424, https://doi.org/10.2788/94128, 2013a.

880 Hiederer, R.: Mapping Soil Typologies - Spatial Decision Support Applied to European Soil Database, Luxembourg: Publications Office of the European Union, 147pp, EUR25932EN Scientific and Technical Research series, ISSN 1831–9424, https://doi.org/doi:10.2788/8728, 2013b.

Hoedt, P. J., Kratzert, F., Klotz, D., Halmich, C., Holzleitner, M., Nearing, G., Hochreiter, S., and Klambauer, G.: MC-LSTM: Mass-Conserving LSTM, arXiv preprint v3, in review, https://arxiv.org/abs/2101.05186v3, 2021.

885 Horn, B. K. P.: Hill shading and the reflectance map, Proceedings of the IEEE, 69(1), 14–47, https://doi.org/10.1109/PROC.1981.11918, 1981.

Hötzl, H.: Origin of the Danube-Aach system, Environmental Geology, 27, 87–96, https://doi.org/10.1007/BF01061676, 1996.

Huscroft, J., Gleeson, T., Hartmann, J., and Börker, J.: Compiling and Mapping Global Permeability of the Unconsolidated 890 and Consolidated Earth: GLobal HYdrogeology MaPS 2.0 (GLHYMPS 2.0), Geophys. Res. Lett., 45, 1897–1904, https://doi.org/10.1002/2017GL075860, 2018.

HZB: Federal Ministry of Agriculture, Regions and Tourism – Hydrographic Central Office, Vienna, Austria (runoff data received: 08.09.2020), 2020.

ICPDR: Danube Basin Facts & Figures, available at:

895   https://www.icpdr.org/flowpaper/viewer/default/files/nodes/documents/icpdr_facts_figures.pdf (last access: 21.09.2020), 2020.

Jain, S. K. and Sudheer, K. P.: Fitting of Hydrologic Models: A Close Look at the Nash–Sutcliffe Index, J. Hydrol. Eng., 13(10), https://doi.org/10.1061/(ASCE)1084-0699(2008)13:10(981), 2008.

Kling, H., Stanzel, P., Fuchs, M., and Nachtnebel, H. P.: Performance of the COSERO precipitation – runoff model under non-

900   stationary conditions in basins with different climates, Hydrological Sciences Journal, 60, 1374–1393, https://doi.org/10.1080/02626667.2014.959956, 2015.

Kling, H., Fuchs, M., and Paulin, M.: Runoff conditions in the upper Danube basin under an ensemble of climate change scenarios, Journal of Hydrology, 424-425, 264–277, https://doi.org/10.1016/j.jhydrol.2012.01.011, 2012.

Kling, H. and Nachtnebel, H. P.: A method for the regional estimation of runoff separation parameters for hydrological

905   modelling, Journal of Hydrology, 364, 163–174, https://doi.org/10.1016/j.jhydrol.2008.10.015, 2009a.

Kling, H. and Nachtnebel, H. P.: A spatio-temporal comparison of water balance modelling in an Alpine catchment, Hydrological Processes, 23, 997–1009, https://doi.org/10.1002/hyp.7207, 2009b.

Klingler, C., Kratzert, F., Schulz, K., and Herrnegger, M.: LamaH-CE | Large-Sample Data for Hydrology and Environmental Sciences for Central Europe – files, Zenodo, https://doi.org/10.5281/zenodo.4525244, 2021.

910 Klingler, C., Bernhardt, M., Wesemann, J., Schulz, K., and Herrnegger, M.: Lokale hydrologische Modellierung mit globalen, alternativen Datensätzen, Hydrologie & Wasserbewirtschaftung, 64(4), 166–187, https://doi.org/10.5675/HyWa_2020.4_1, 2020.

Knoben, W. J. M., Freer, J. E., and Ross, A. W.: Technical note: Inherent benchmark or not? Comparing Nash–Sutcliffe and Kling–Gupta efficiency scores, Hydrol. Earth Syst. Sci., 23, 4323–4331, https://doi.org/10.5194/hess-23-4323-2019,

915   2019.

Kobolschnig, G. R. and Schöner, W.: The relevance of glacier melt in the water cycle of the Alps: the example of Austria, Hydrol. Earth Syst. Sci., 15, 2039–2048, https://doi.org/10.5194/hess-15-2039-2011, 2011.

Kratzert, F., Klotz, D., Herrnegger, M., Sampson, A. K., Hochreiter, S., and Nearing, G.: Toward improved predictions in ungauged basins: Exploiting the power of machine learning, Water Resources Research, 55, 11344–11354,

920   https://doi.org/10.1029/2019WR026065, 2019a.

Kratzert, F., Klotz, D., Shalev, G., Klambauer, G., Hochreiter, S., and Nearing, G.: Towards learning universal, regional, and local hydrological behaviors via machine learning applied to large-sample datasets, Hydrol. Earth Syst. Sci., 23, 5089–5110, https://doi.org/10.5194/hess-23-5089-2019, 2019b.

Kratzert, F., Klotz, D., Brenner, C., Schulz, K., and Herrnegger, M.: Rainfall-runoff modelling using Long Short-Term

925   Memory (LSTM) networks, Hydrol. Earth Syst. Sci., 22, 6005–6022, https://www.hydrol-earth-syst-sci.net/22/6005/2018, 2018.

Kuhn, M.: The Reaction of Austrian Glaciers and their Runoff to Changes in Temperature and Precipitation Levels, Österreichische Wasser- und Abfallwirtschaft, 56(1–2), 1–7, 2004.

Kuentz, A., Arheimer, B., Hundecha, Y., and Wagener, T.: Understanding hydrologic variability across Europe through

930   catchment classification, Hydrol. Earth Syst. Sci., 21, 2863–2879, https://doi.org/10.5194/hess-21-2863-2017, 2017.

Ladson, A., Brown, R., Neal, B., and Nathan, R.: A standard approach to baseflow separation using the Lyne and Hollick filter, Australian Journal of Water Resources, 17, 25–34, https://doi.org/10.7158/13241583.2013.11465417, 2013.

Lambrecht, A. and Kuhn, M.: Glacier changes in the Austrian Alps during the last three decades, derived from the new Austrian glacier inventory, Ann. Glaciol., 46, 177–184, https://doi.org/10.3189/172756407782871341, 2007.

935   Lehner, B., Liermann, C., Revenga, C., Vörösmarty, C., Fekete, B., et al.: High-resolution mapping of the world's reservoirs and dams for sustainable river-flow management, Front. Ecol. Environ., 9(9), 494–502, https://doi.org/10.1890/100125, 2011.

Lehner, B., Verdin, K., and Jarvis, A.: New global hydrography derived from spaceborne elevation data, Eos, Transactions, AGU, 89(10), 93–94, https://doi.org/10.1029/2008EO100001, 2008.

940   Linke, S., Lehner, B., Ouellet Dallaire, C., Ariwi, J., Grill, G., Anand, M., Beames, P., Burchard-Levine, V., Maxwell, S., Moidu, H., Tan, F., and Thieme, M.: Global hydro-environmental sub-basin and river reach characteristics at high spatial resolution, Scientific Data, 6, 283, https://doi.org/10.1038/s41597-019-0300-6, 2019.

LUBW: State Agency for the Environment Baden-Württemberg – Hydrographic Service, Karlsruhe, Germany, available at: http://udo.lubw.baden-wuerttemberg.de/public/p/pegel_messwerte_leer (runoff data received: 04.09.2020), 2020.

945   Luke, A., Vrugt, J. A., AghaKouchak, A., Matthew, R., and Sanders, B. F.: Predicting nonstationary flood frequencies: Evidence supports an updated stationarity thesis in the United States, Water Resour. Res., 53, 5469–5494, https://doi.org/10.1002/2016WR019676, 2017.

McCuen, R. H., Knight, Z., and Cutter, G.: Evaluation of the Nash–Sutcliffe Efficiency Index, J. Hydrol. Eng., 11(6), https://doi.org/10.1061/(ASCE)1084-0699(2006)11:6(597), 2006.

950   McMillan, H., Krueger, T., and Freer, J.: Benchmarking observational uncertainties for hydrology: rainfall, river discharge and water quality, Hydrol. Process., 26, 4078–4111, https://doi.org/10.1002/hyp.9384, 2012.

Mehdi, B., Dekens, J., and Herrnegger, M.: Climatic impacts on water resources in a tropical catchment in Uganda and adaptation measures proposed by resident stakeholders, Clim. Change, 164, https://doi.org/10.1007/s10584-021-02958-9, 2021.

955   Mulligan, M., van Soesbergen, A., and Saenz, L.: GOODD, a global dataset of more than 38,000 georeferenced dams, Sci. Data, 7(31), https://doi.org/10.1038/s41597-020-0362-5, 2020.

Muñoz Sabater, J., Dutra, E., Agustí-Panareda, A., Albergel, C., Arduini, G., Balsamo, G., Boussetta, S., Choulga, M., Harrigan, S., Hersbach, H., Martens, B., Miralles, D. G., Piles, M., Rodríguez-Fernández, N. J., Zsoter, E., Buontempo, C., and Thépaut, J. N.: ERA5-Land: A state-of-the-art global reanalysis dataset for land applications, Earth Syst. Sci. Data Discuss. [preprint], in review, https://doi.org/10.5194/essd-2021-82, 2021.

Muñoz Sabater, J.: ERA5-Land hourly data from 1981 to present, Copernicus Climate Change Service (C3S) Climate Data Store (CDS), available at: https://doi.org/10.24381/cds.e2161bac (last access: 22.10.2020), 2019a.

Muñoz Sabater, J.: First ERA5-Land dataset to be released this spring, ECMWF newsletter, number 159 - spring 2019, available at: https://www.ecmwf.int/en/newsletter/159/news/first-era5-land-dataset-be-released-spring (last access: 30.11.2020), 2019b.

Muñoz Sabater, J., Dutra, E., Balsamo, G., Hersbach, H., Boussetta, S., Dee, D., and Hirahara, S.: ERA5-Land: A new state-of-the-art Global Land Surface Reanalysis Dataset, 31st Conference on Hydrology – 2017 AMS annual meeting, Seattle, US, 2017.

Myneni, R., Knyazikhin, Y., and Park, T.: MCD15A3H MODIS/Terra+Aqua Leaf Area Index/FPAR 4-day L4 Global 500m SIN Grid V006 [Data set], NASA EOSDIS Land Processes DAAC, available at: https://doi.org/10.5067/MODIS/MCD15A3H.006 (last access: 12.03.2020), 2015.

Nachtnebel, H. P., and Fuchs, M.: Assessment of hydrological changes in Austria due to possible climate change (in German), Österreichische Wasser- und Abfallwirtschaft, 56(7/8), 79–92, 2004.

Nachtnebel, H. P., Baumung, S., and Lettl, W.: Abflussprognosemodell für das Einzugsgebiet der Enns und Steyr (in German), Report, Institute for Water Management, Hydrology and Hydraulic Engineering, University of Natural Resources and Applied Life Sciences, Vienna, Austria, 1993.

Nash, J. E. and Sutcliffe, J. V.: River flow forecasting through conceptual models part I - A discussion of principles, J. Hydrol., 10(3), 282–290, https://doi.org/10.1016/0022-1694(70)90255-6, 1970.

Nearing, G. S., Kratzert, F., Sampson, A. K., Pelissier, C. S., Klotz, D., Frame, J. M., Prieto, C., and Gupta, H. V.: What Role Does Hydrological Science Play in the Age of Machine Learning?, Water Resour. Res., e2020WR028091, https://doi.org/10.1029/2020wr028091, 2020.

Newman, A. J., Clark, M. P., Sampson, K., Wood, A., Hay, L. E., Bock, A., Viger, R. J., Blodgett, D., Brekke, L., Arnold, J. R., Hopson, T., and Duan, Q.: Development of a large-sample watershed-scale hydrometeorological data set for the contiguous USA: data set characteristics and assessment of regional variability in hydrologic model performance, Hydrol. Earth Syst. Sci., 19, 209–223, https://doi.org/10.5194/hess-19-209-2015, 2015.

Panagos, P., Van Liedekerke, M., Jones, A., and Montanarella L.: European Soil Data Centre: Response to European policy support and public data requirements, Land Use Policy, 29(2), 329–338, https://doi.org/10.1016/j.landusepol.2011.07.003, 2012.

Panagos, P.: The European soil database, GEO: connexion, 5(7), 32–33, 2006.

990 Pelletier, J. D., Broxton, P. D., Hazenberg, P., Zeng, X., Troch, P. A., Niu, G., Williams, Z. C., Brunke, M. A., and Gochis, D.: Global 1-km Gridded Thickness of Soil, Regolith, and Sedimentary Deposit Layers. ORNL DAAC, Oak Ridge, Tennessee, USA, https://doi.org/10.3334/ORNLDAAC/1304, 2016.

Prohaska, S., Brilly, M., and Kryžanowski, A.: Cooperation of hydrologists from the Danube River Basin, Hydrol. Earth Syst. Sci. Discuss., 1–10, https://doi.org/10.5194/hess-2020-66, 2020.

995 Python Software Foundation: Python Language Reference, available at https://www.python.org, 2020.

QGIS Development Team: QGIS Geographic Information System, Open Source Geospatial Foundation Project, available at: http://qgis.org, 2020.

Olden, J. D. and Poff, N. L.: Redundancy and the choice of hydrologic indices for characterizing streamflow regimes, River Res. Appl., 19, 101–121, https://doi.org/10.1002/rra.700, 2003.

1000 Oerlemans, J., Anderson, B., Hubbard, A., Huybrechts, P., Johannesson, T., Knap, W. H., Schmeits, M., Stroeven, A. P., van de Wal, R. S. W., and Wallinga, J.: Modelling the response of glaciers to climate warming, Clim. Dynam., 14/4, 267–274, https://doi.org/10.1007/s003820050222, 1998.

R Core Team: R: A language and environment for statistical computing, R Foundation for Statistical Computing, Vienna, Austria, available at: https://www.r-project.org, 2020.

1005 Sankarasubramanian, A., Vogel, R. M., and Limbrunner, J. F.: Climate elasticity of streamflow in the United States, Water Resour. Res., 37, 1771–1781, https://doi.org/10.1029/2000WR900330, 2001.

Sawicz, K., Wagener, T., Sivapalan, M., Troch, P. A., and Carrillo, G.: Catchment classification: empirical analysis of hydrologic similarity based on catchment function in the eastern USA, Hydrol. Earth Syst. Sci., 15, 2895–2911, https://doi.org/10.5194/hess-15-2895-2011 , 2011.

1010 Schaake, J. C., Hamill, T. M., Buizza, R., and Clark, M.: HEPEX: the hydrological ensemble prediction experiment, Bulletin of the American Meteorological Society, 88(10), 1541–1548, https://doi.org/10.1175/BAMS-88-10-1541, 2007.

Schaefli, B. and Gupta, H. V.: Do Nash values have value?, Hydrol. Process., 21(15), 2075–2080, https://doi.org/10.1002/hyp.6825, 2007.

Schulz, K., Herrnegger, M., Wesemann, J., Klotz, D., and Senoner, T: Kalibrierung COSERO-Mur für ProVis. (in German), 1015 Final report, Institute for Water Management, Hydrology and Hydraulic Engineering, University of Natural Resources and Life Science, Vienna, Austria, 2016.

Schumm, S. A.: Evolution of drainage systems and slopes in Badlands at Perth Amboy, New Jersey, GSA Bulletin, 67(5), 597–646, https://doi.org/10.1130/0016-7606(1956)67[597:EODSAS]2.0.CO;2, 1956.

Singh, R., Archfield, S. A., and Wagener, T.: Identifying dominant controls on hydrologic parameter transfer from gauged to 1020 ungauged catchments – A comparative hydrology approach, J. Hydrol., 517, 985–996, https://doi.org/10.1016/j.jhydrol.2014.06.030, 2014.

Sit, M., Demiray, B. Z., Xiang, Z., Ewing, G. J., Sermet, Y., and Demir, I.: A comprehensive review of deep learning applications in hydrology and water resources, Water Sci. Technol., 82(12), 2635–2670, https://doi.org/10.2166/wst.2020.369, 2020.

1025 Smith, M. B., Seo, D. J., Koren, V. I., Reed, S. M., Zhang, Z., Duan, Q., Moreda, F., and Cong, S.: The Distributed Model Intercomparison Project (DMIP): motivation and experiment design, J. Hydrol., 298, 4–26, https://doi.org/10.1016/j.jhydrol.2004.03.040, 2004.

Stanzel, P. and Nachtnebel, H. P.: Potential climate change impact on Austria's water balance and hydro-power industry (in German), Österreichische Wasser- und Abfallwirtschaft, 62(9/10), 180–187, https://doi.org/10.1007/s00506-010-0234-x, 2010.

1030

Stanzel, P., Kahl, B., Haberl, U., Herrnegger M., and Nachtnebel, H. P.: Continuous hydrological modelling in the context of real time flood forecasting in alpine Danube tributary catchments, IOP Conference Series: Earth and Environmental Science, 4(1): 012005, https://doi.org/10.1088/1755-1307/4/1/012005, 2008.

Tallaksen, L. and Van Lanen, H. A. J.: Hydrological drought. Processes and estimation methods for streamflow and groundwater, Developments in Water Science, 48, ISSN: 0167-5648, Amsterdam: Elsevier, 579pp, 2004.

1035

Thornthwaite, C. W. and Mather, J. R.: Instructions and tables for computing potential evapotranspiration and the water balance, Publications in Climatology, 10(3), 311pp, Laboratory of Climatology, Drexel Institute of Technology, New Jersey, 1957.

Tolson, B. A. and Shoemaker, C. A.: Dynamically dimensioned search algorithm for computationally efficient watershed model calibration, Water Resources Research, 43(1), https://doi.org/10.1029/2005WR004723, 2007.

1040

Toth, B., Weynants, M., Pasztor, L., and Hengl, T.: 3D soil hydraulic database of Europe at 250 m resolution, Hydrological Processes, 31, 2662–2666, https://doi.org/10.1002/hyp.11203, 2017.

Toth, B., Weynants, M., Nemes, A., Makó, A., Bilas, G., and Toth, G.: New generation of hydraulic pedotransfer functions for Europe, European Journal of Soil Science, 66, 226–238, https://doi.org/10.1111/ejss.12192, 2015.

1045 Trabucco, A. and Zomer, R.: Global Aridity Index and Potential Evapotranspiration (ET0) Climate Database v2, CGIAR Consortium for Spatial Information (CGIAR-CSI), published online, available at: https://doi.org/10.6084/m9.figshare.7504448.v3 (last access: 18.03.2020), 2019.

TYROL: Catalog Water Network Tyrol, Government of the Austrian federal state Tyrol, Innsbruck, available at: https://www.data.gv.at/katalog (downloaded: 17.10.2020), 2020.

1050 Van Lanen, H. A. J., Wanders, N., Tallaksen, L. M., and Van Loon, A. F.: Hydrological drought across the world: impact of climate and physical catchment structure, Hydrol. Earth Syst. Sci., 17, 1715–1732, https://doi.org/10.5194/hess-17-1715-2013, 2013.

Vermote, E.: MOD09Q1 MODIS/Terra Surface Reflectance 8-Day L3 Global 250m SIN Grid V006 [Data set], NASA EOSDIS Land Processes DAAC, available at: https://doi.org/10.5067/MODIS/MOD09Q1.006 (last access: 12.03.2020), 2015.

1055

Warszawski, L., Frieler, K., Huber, V., Piontek, F., Serdeczny, O., and Schewe, J.: The inter-sectoral impact model intercomparison project (ISI–MIP): project framework, Proceedings of the National Academy of Sciences, 111(9), 3228–3232, https://doi.org/10.1073/pnas.1312330110, 2014.

Wesemann, J., Herrnegger, M., and Schulz, K.: Hydrological modelling in the anthroposphere: predicting local runoff in a heavily modified high-alpine catchment, Journal of Mountain Sciences, 15(5), 921–938, https://doi.org/10.1007/s11629-017-4587-5, 2018.

Westerberg, I. K., Wagener, T., Coxon, G., McMillan, H. K., Castellarin, A., Montanari, A., and Freer, J.: Uncertainty in hydrological signatures for gauged and ungauged catchments, Water Resour. Res., 52, 1847–1865, https://doi.org/10.1002/2015WR017635, 2016.

Westerberg, I. K. and McMillan, H. K.: Uncertainty in hydrological signatures, Hydrol. Earth Syst. Sci., 19, 3951–3968, https://doi.org/10.5194/hess-19-3951-2015, 2015.

WGMS (World Glacier Monitoring Service), Glacier Mass Balance Bulletin, No. 8 (2002–2003), edited by: Haeberli, W., Noetzli, J., Zemp, M., Baumann, S., Frauenfelder, R., Hoelzle, M., Department of Geography, University of Zürich, 100pp, 2005.

Woods, R. A.: Analytical model of seasonal climate impacts on snow hydrology: Continuous snowpacks, Adv. Water Resour., 32, 1465–1481, https://doi.org/10.1016/j.advwatres.2009.06.011, 2009.

Yang, X. and Giusti, M.: ERA5-Land: data documentation, CDS dataset documentation, European Centre for Medium-Range Weather Forecasts (ECMWF), available at: https://confluence.ecmwf.int/display/CKB/ERA5-Land%3A+data+documentation (last access: 30.11.2020), 2020.

Yokoo, Y. and Sivapalan, M.: Towards reconstruction of the flow duration curve: development of a conceptual framework with a physical basis, Hydrol. Earth Syst. Sci., 15, 2805–2819, https://doi.org/10.5194/hess-15-2805-2011, 2011.

Appendix A

Table A1: Gauge referred attributes.

Attribute	Description	Unit	References
ID	ID number, which is used for linking between all the different files	-	-
govnr	Official gauge number from the associated governments	-	BAFU (2020), CHMI (2020), GKD (2020), HZB (2020), LUBW (2020)
name	Official name of the runoff gauge	-	see above
river	Name of the belonging river	-	see above

area_gov	Catchment area obtained from the administration	km^2	see above
elev	Elevation of the gauge`s zero point	m a.s.l.	see above
lon	Longitude in LAEA Europe grid (EPSG 3035)	m	see above
lat	Latitude in LAEA Europe (EPSG 3035)	m	see above
country	ISO 3166 ALPHA-3 code for country	-	see above
fedstate	Abbreviation for federal state; water management administration is executed in the given countries at the stage of federal states [a]	-	see above
region	River-based region [b]	-	see above
obsbeg_day	Start of daily runoff time series in the dataset	year	see above
obsbeg_hr	Start of continuous (hourly) runoff data recording	year	see above
obsend	End of continuous (hourly) runoff data recording; number 0 indicates an up-to-date recording; daily time series might last longer	year	see above
gaps_pre	Fraction of gaps in the raw hourly runoff time series	‰	see above
gaps_post	Fraction of gaps in the hourly runoff time series after our processing (linear interpolation, up to 6h)	‰	see above
area_ratio	Ratio between variable "area_calc" of basin delineation A (Table A3) and "area_gov"	-	BAFU (2020), CHMI (2020), GKD (2020), HZB (2020), LUBW (2020), HAO (2007), HydroATLAS (Linke et al., 2019)
nrs_euhyd	"OBJECT_ID" of the next river segment from stream network "EU-Hydro – River Network Database" [f]	-	EU-Hydro – River Network Database (EEA, 2019)
nrs_rivat	"HYRIV_ID" of the next river segment from stream network "RiverATLAS" [f]	-	HydroATLAS (Linke et al., 2019)
HIERARCHY	Gauge hierarchy [c]	-	see above
NEXTUPID	ID of the next upstream gauges (can be one or more), 0 indicates no upstream gauges [c]	-	see above
NEXTDOWNID	ID of the next downstream gauge (only one); 0 indicates no downstream gauge [c]	-	see above
dist_hup	Horizontal stream length from the most distant beginning of a watercourse within the basin to the gauge [d]	km	BAFU (2020), CHMI (2020), GKD (2020), HZB (2020), LUBW (2020), EU-Hydro –

			River Network Database (EEA, 2019)
dist_hdn	Horizontal stream length from the actual gauge to the next downstream gauge [c]	km	see above
elev_diff	Elevation difference from the actual`s gauge zero point to the next downstream`s gauge zero point [c]	m	see above
strm_slope	Slope of the actual gauge to the next downstream`s gauge; fraction of "elev_diff" and "dist_hdn" [c]	m km^{-1}	see above
ckhs	Declares if a timestep in the runoff time series was checked by the staff of the hydrological services or not; the specific scope of the check is not described [e]	0 (False) or 1 (True)	BAFU (2020), CHMI (2020), GKD (2020), HZB (2020), LUBW (2020)
qceq	QC flag which is set, if runoff remains equal in at least 10 consecutive time steps (daily or hourly); section 2.3 in Gudmundsson et al. (2018) [e]	0 or 1	see above
qcol	QC flag which is set, if runoff value is classified as outlier; values which are declared as outliers can also be low/high flows in rare cases; section 2.3 in Gudmundsson et al. (2018) [e]	0 or 1	see above

[a] List of abbrev. for attribute fedstate: Austria (BLD – Burgenland, CRN – Carinthia, LAT – Lower Austria, SBG – Salzburg, STY – Styria, TYR – Tyrol, UAT – Upper Austria, VBG – Vorarlberg, VIE – Vienna); Germany (BAV – Bavaria, BWT – Baden-Württemberg); Switzerland (GRI – Grisons, STG – Saint Gallen); Liechtenstein (LIE - Liechtenstein); Czech Republic (OLM – Olomouc, SBO – South Bohemian, SMO – South Moravian, VYS – Vysočina, ZLN - Zlin). [b] List of abbrev. for attribute region: 1 – Rhine, 2 – Danube above Inn, 3 – Inn above Salzach, 4 – Salzach, 5 – Inn under Salzach, 6 – Danube between Inn and Traun, 7 – Traun, 8 – Danube between Traun and Enns, 9 – Enns, 10 – Danube between Enns and Morava, 11 – Vltava, 12 – Morava, 13 – Danube between Morava and Leitha, 14 – Leitha, 15 – Rabniz, 16 – Raab, 17 – Mur, 18 – Drava. [c] Only for basin delineation B and C. [d] Only for basin delineation A. [e] Visible in daily and hourly runoff time series. [f] End of the river segment (to which the attributes within the river network refer) can sometimes be rather far from the gauge. If a single river segment extended over several gauges, the ID of the river segment was only indicated at the most downstream gauge.

Table A2: Meteorological variables from ERA5-Land dataset (Muñoz Sabater, 2019a).

Variable hourly	Daily aggregation	Description	Unit

DOY	unchanged	Day of year	-
HOD	omitted	Hour of day	-
2m_temp	max, mean, min	Air temperature at a height of 2 m above Earth surface	°C
2m_dp_temp	max, mean, min	Dewpoint temperature at a height of 2 m above Earth surface	°C
10m_wind_u	mean	Horizontal speed of air moving towards the east at a height of 10 m above Earth surface	m s^{-1}
10m_wind_v	mean	horizontal speed of air moving towards the north at a height of 10 m above Earth surface	m s^{-1}
fcst_alb	mean	Forecast albedo, fraction of solar (shortwave) radiation reflected by Earth's surface (direct and diffuse)	-
lai_high_veg	mean	One-half of the total green leaf area per unit horizontal ground surface area for high vegetation type	-
lai_low_veg	mean	One-half of the total green leaf area per unit horizontal ground surface area for low vegetation type	-
swe	mean	Water equivalent of snow	mm
surf_net_solar_rad	max, mean	Amount of solar radiation (shortwave radiation) reaching the Earth`s surface (direct and diffuse) minus the amount reflected by the Earth's surface (governed by albedo); positive sign is indicator for radiation to the Earth	W m^{-2}
surf_net_therm_rad	max, mean	Net thermal radiation at the Earth´s surface; positive sign is indicator for radiation from the Earth	W m^{-2}
surf_press	mean	Surface pressure	Pa
total_et	sum	Total evapotranspiration, positive values indicate evapotranspiration, negative values condensation	mm
prec	sum	Total amount of precipitation (liquid and frozen)	mm
volsw_123	mean	Fraction of water in top soil layer; 0 to 100 cm depth	m^3 m^{-3}
volsw_4	mean	Fraction of water in sub soil layer; 100 to 289 cm depth	m^3 m^{-3}

Table A3: Topographic indices.

Attribute	Description	Unit	Data source
area_calc	Calculated basin area	km^2	HAO (2007), HydroATLAS (Linke et al., 2019)

elev_mean	Mean catchment elevation [a]	m a.s.l.	NASA JPL SRTMGL1 V3 Digital Elevation 30m (Farr et al., 2007)
elev_med	Median catchment elevation [a]	m a.s.l.	see above
elev_std	Standard deviation of elevation in catchment [a]	m a.s.l.	see above
elev_ran	Range of catchment elevation (max. – min. elev.) [a]	m a.s.l.	see above
slope_mean	Mean catchment slope; Horn (1981) [a]	m km^{-1}	see above
mvert_dist	Horizontal distance from the farthest point of the catchment to the belonging gauge (length axis)	km	BAFU (2020), CHMI (2020), GKD (2020), HZB (2020), LUBW (2020)
mvert_ang	Angle between North direction and connection from farthest point of catchment to belonging gauge (length axis); e.g. direction from north (farthest catchment point) to south (gauge): 180°, direction from east to west: 270°	degree	see above
elon_ratio	Elongation ratio R_e after Schumm (1956); ratio between the diameter D of an equivalent circle and the area of the catchment area to its length L (mvert_dist), $$R_e = \frac{1}{L} \times \sqrt{\frac{4 \times A}{\pi}} = \frac{D}{L}$$	-	see above
strm_dens	Stream density D_F, ratio of lengths of streams L_F and the catchment area A (area_calc), $D_F = \frac{\sum L_F}{A}$	km km^{-2}	EU-Hydro – River Network Database (EEA, 2019)

[a] Upscaling approach 2.

1095

Table A4: Climatic indices.

Attribute	Description	Unit	Data source
p_mean	Mean daily precipitation [a,d]	mm day^{-1}	ERA5L (Muñoz Sabater, 2019a)
et0_mean	Mean daily reference evapotranspiration ET0 [b,e]	mm day^{-1}	Global Aridity Index and Potential Evapotranspiration (ET0) Climate Database v2 (Trabucco and Zomer, 2019)
eta_mean	Mean daily total evapotranspiration [a,d]	mm day^{-1}	ERA5L (Muñoz Sabater, 2019a)

arid_1	Aridity, computed as the ratio of mean ET0 [b,e] (from Climate Database v2) and mean precipitation [a,d] (from ERA5-Land)	-	ERA5L (Muñoz Sabater, 2019a), Global Aridity Index and Potential Evapotranspiration (ET0) Climate Database v2 (Trabucco and Zomer, 2019)
arid_2	Reciprocal value of aridity index from Climate Database v2 [b,e]	-	Global Aridity Index and Potential Evapotranspiration (ET0) Climate Database v2 (Trabucco and Zomer, 2019)
p_season	Seasonality and timing of precipitation (estimated using sine curves) to represent the annual precipitation cycles, positive (negative) values indicate that precipitation sums are higher during summer (winter) months; values close to 0 indicate uniform precipitation throughout the year; Eq. (14) in Woods (2009) [a,d]	-	see above
frac_snow	Fraction of precipitation falling as snow, i.e. falling on days with mean temperature below 0 °C [a,d]	-	see above
hi_prec_fr	Frequency of high precipitation days (≥ 5 times mean daily precipitation) [a,d]	days yr^{-1}	see above
hi_prec_du	Mean duration of high precipitation events (number of consecutive days with ≥ 5 times mean daily precipitation) [a,d]	days	see above
hi_prec_ti	Season during which most high precipitation days (≥ 5 times mean daily precipitation) occur [a,d]	season [c]	see above
lo_prec_fr	Frequency of dry days (< 1 mm day^{-1} precipitation) [a,d]	days yr^{-1}	see above
lo_prec_du	Mean duration of dry periods (number of consecutive days with < 1 mm day^{-1} precipitation) [a,d]	days	see above
lo_prec_ti	Season during which most dry days (< 1 mm day^{-1} precipitation) occur [a,d]	season [c]	see above

[a] Period 1 October 1989 to 30 September 2009. [b] Period 1970 to 2000. [c] List of abbrev. for season: djf – December/January/February, mam – March/April/May, jja – June/July/August, son – September/October/November. [d] Upscaling approach 1. [e] Upscaling approach 2.

1100

Table A5: Hydrological signatures.

Attribute	Description	Unit	Data source
q_mean	Mean daily runoff [a,c,d]	mm day^{-1}	BAFU (2020), CHMI (2020), GKD (2020), HZB (2020), LUBW (2020)
runoff_ratio	Runoff ratio, computed as the ratio of mean daily runoff and mean daily precipitation [a,b,c,d]	-	BAFU (2020), CHMI (2020), GKD (2020), HZB (2020), LUBW (2020), ERA5L (Muñoz Sabater, 2019a)
stream_elas	Runoff-precipitation elasticity, i.e. the sensitivity of runoff to changes in precipitation at the annual timescale, using the mean daily runoff as reference; Eq. (7) in Sankarasubramanian et al. (2001), with the last element being $\bar{P} / \bar{Q}$ not $\bar{Q} / \bar{P}$ [a,c,d]	-	BAFU (2020), CHMI (2020), GKD (2020), HZB (2020), LUBW (2020)
slope_fdc	Slope of the flow duration curve between the log-transformed 33rd and 66th runoff percentiles; Eq. (3) in Sawicz et al. (2011) [a,c,d]	-	see above
baseflow_index _ladson	Baseflow index, computed as the ratio of mean daily baseflow and mean daily discharge; hydrograph separation is performed using the Ladson et al. (2013) digital filter [a,c,d]	-	see above
baseflow_index _lfstat	equal than above, but hydrograph separation is performed using a package from Tallaksen and Van Lanen (2004) [a,c,d]	-	see above
hfd_mean	Mean half-flow date, i.e. number of days since the beginning of the hydrological year (1 October) on which the accumulated runoff reaches half of the annual volume; Court (1962) [a,c,d]	days since 1 October	see above
Q5	5% flow quantile (low flow) [a,c,d]	mm day^{-1}	see above
Q95	95% flow quantile (high flow) [a,c,d]	mm day^{-1}	see above
high_q_freq	Frequency of high-flow days (> 9 times median daily flow); Clausen and Biggs (2000), Table 2 in Westerberg and McMillan (2015) [a,c,d]	days yr^{-1}	see above

high_q_dur	Mean duration of high-flow events (number of consecutive days > 9 times median daily flow); Clausen and Biggs (2000), Table 2 in Westerberg and McMillan (2015) [a,c,d]	days	see above
low_q_freq	Frequency of low-flow days (< 0.2 times mean daily flow); Olden and Poff (2003), Table 2 in Westerberg and McMillan (2015) [a,c,d]	days yr^{-1}	see above
low_q_dur	Mean duration of low-flow events (number of consecutive days < 0.2 times mean daily flow); Olden and Poff (2003), Table 2 in Westerberg and McMillan (2015) [a,c,d]	days	see above
zero_q_freq	Percentage of days with no discharge [a,c,d]	%	see above

[a] Period 1 October 1989 to 30 September 2009 and additionally from the first 1 October in the time series after 1981 to 30 September 2017. [b] Upscaling approach 1. [c] No values if there are more than 5% gaps in the calculation period. [d] No values for basins / gauges which are attributed with degimpact = "x".

1105

Table A6: Land cover characteristics.

Attribute	Description	Unit	Data source
lc_dom	3-digit short code of dominant land cover class [a,b]	-	CORINE (2012)
agr_fra	Fraction of agricultural areas (all CLC classes starting with number 2) [a,b]	-	see above
bare_fra	Fraction of bare areas (CLC classes 332, 333) [a,b]	-	see above
forest_fra	Fraction of forest areas (CLC classes 311, 312, 313) [a,b]	-	see above
glac_fra	Fraction of glaciers (CLC class 335) [a,b]	-	see above
lake_fra	Fraction of natural or artificial water bodies with all-season water filling (CLC class 512) [a,b]	-	see above
urban_fra	Fraction of areas mainly occupied by buildings including their connected areas (CLC classes 111, 112, 121, 122, 123, 124) [a,b]	-	see above

[a] Upscaling approach 2. [b] Land class nomenclature is listed in the folder "G_appendix".

Table A7: Vegetation indices.

Attribute	Description	Unit	Data source

lai_max	Maximum monthly mean of one-sided leaf area index (based on 12 monthly means) [a]	-	MODIS MCD15A3H (Myneni et al., 2015)
lai_diff	Difference between maximum and minimum monthly mean of one-sided leaf area index (based on 12 monthly means) [a]	-	see above
ndvi_max	Maximum monthly mean of NDVI (based on 12 monthly means) [a]	-	MODIS MOD09Q1 (Vermote, 2015)
ndvi_min	Minimum monthly mean of NDVI (based on 12 monthly means) [a]	-	see above
gvf_max	Maximum monthly mean of the green vegetation fraction (based on 12 monthly means) [a]	-	MODIS MOD09Q1 (Vermote, 2015), MODIS MCD12Q1 (Friedl and Sulla-Menashe, 2019)
gvf_diff	Difference between the maximum and minimum monthly mean of the green vegetation fraction (based on 12 monthly means) [a]	-	see above

1110   [a] Upscaling approach 2.

Table A8: Soil characteristics.

Attribute	Description	Unit	Data source
bedrk_dep	Depth to bedrock; maximum is 50 m [c]	m	Pelletier et al. (2016)
root_dep	Depth available for roots; maximum is 1.5 m [a,c]	m	European Soil Database Derived data (Hiederer, 2013a/b)
soil_poros	Total soil porosity [a,b,c]	-	see above
soil_condu	Saturated hydraulic conductivity; maximum is 2 m [a,b,c]	cm hr^{-1}	3D Soil Hydraulic Database of Europe (Toth et al., 2017)
soil_tawc	Total available water content (between field capacity and permanent wilting point) [a,b,c]	m	European Soil Database Derived data (Hiederer, 2013a/b)
sand_fra	Sand fraction (of soil material < 2 mm) [a,b,c]	-	see above
silt_fra	Silt fraction (of soil material < 2 mm) [a,b,c]	-	see above
clay_fra	Clay fraction (of soil material < 2 mm) [a,b,c]	-	see above
grav_fra	Fraction of gravel (of overall soil) [a,b,c]	-	see above
oc_fra	Fraction of organic material (of overall soil) [a,b,c]	-	see above

1115

Table A9: Geologic attributes.

Attribute	Description	Unit	Data source
gc_dom	Dominant geologic class [a]	-	GLiM (Hartmann and Moosdorf, 2012)
gc_ig_fra	Fraction of "ice and glacier" (ig) [a]	-	see above
gc_mt_fra	Fraction of "metamorphites" (mt) [a]	-	see above
gc_pa_fra	Fraction of "acid plutonic rocks" (pa) [a]	-	see above
gc_pb_fra	Fraction of "basic plutonic rocks" (pa) [a]	-	see above
gc_pi_fra	Fraction of "intermediate plutonic rocks" (pi) [a]	-	see above
gc_py_fra	Fraction of "pyroclastics" (py) [a]	-	see above
gc_sc_fra	Fraction of "carbonate sedimentary rocks" (sc) [a]	-	see above
gc_sm_fra	Fraction of "mixed sedimentary rocks" (sm) [a]	-	see above
gc_ss_fra	Fraction of "siliciclastic sedimentary rocks" (ss) [a]	-	see above
gc_su_fra	Fraction of "unconsolidated sediments" (su) [a]	-	see above
gc_va_fra	Fraction of "acid volcanic rocks" (va) [a]	-	see above
gc_vb_fra	Fraction of "basic volcanic rocks" (vb) [a]	-	see above
gc_wb_fra	Fraction of "water bodies" (wb) [a]	-	see above
geol_perme	Subsurface permeability (log10) [b]	-	GLHYMPS (Gleeson et al., 2014)
peol_poros	Subsurface porosity [b]	-	see above

ᵃ Upscaling approach 1. ᵇ Upscaling approach 2.

Table A10: Attributes in the accompanying file "Water_balance.csv" ᵉ

Attribute	Description	Unit	Data source
P	Mean precipitation of ERA5-Land [a,b]	mm d⁻¹	ERA5L (Muñoz Sabater, 2019a)
PCRPS	Mean precipitation of CHIPRS Daily v2.0 [a,b]	mm d⁻¹	CHIRPS Daily v2.0 (Funk et at., 2015)
PERA5	Mean precipitation of ERA5 [a,b]	mm d⁻¹	ERA5 (Hersbach et al., 2020)
PMSW	Mean precipitation of MSWEP v2.2 [a,b]	mm d⁻¹	MSWEP v2.2 (Beck et al., 2017; 2019)

PET	Mean PET of ERA5-Land [a,b]	mm d^{-1}	ERA5L (Muñoz Sabater, 2019a)
ET0	Mean ET0 of Climate Database v2 [a,c]	mm d^{-1}	Global Aridity Index and Potential Evapotranspiration (ET0) Climate Database v2 (Trabucco and Zomer, 2019)
ETA	Mean actual evapotranspiration of ERA5-Land [a,b]	mm d^{-1}	ERA5L (Muñoz Sabater, 2019a)
Q1	Mean runoff height [b,f,h]	mm d^{-1}	BAFU (2020), CHMI (2020), GKD (2020), HZB (2020), LUBW (2020)
Q2	Mean runoff height [d,g,h]	mm d^{-1}	see above

1120 [a] Computed for basin delineation A. [b] Period 1 October 1989 to 30 September 2009. [c] Period 1970 to 2000. [d] Period from the first 1 October in the time series after 1981 to 30 September 2017. [e] No values, where corresponding gauge is attributed with "degimpact" = x (Table 1). [f] No values for gauges, whose time series do not cover the full period. [g] Values only if at least 5 years of observations are available. [h] No values if there are more than 5% gaps in the calculation period.

1125 **Table A11: Attributes in the accompanying file "Crossbasin_water_transfers.csv" [a]**

Attribute	Description	Unit
ID	ID of sourcing basin	-
To_ID	ID of receiving basin	-
cross_region	Flag if river region (Fig. 1, Table B1) is crossed (0 - no, 1 - yes)	-
lower_thres	Lower threshold for water cross-basin transfer	m^3 s^{-1}
upper_thres	Upper threshold for water cross-basin transfer	m^3 s^{-1}
estimated	Flag if "lower_thres" and "lower_thres" are estimated (1) due to lack of publicly available information; otherwise this information is taken from governmental registers, system specifications, etc. (0)	-
model	Flag if the cross-basin transfer is implemented in the hydrological model COSERO (0 - no, 1 - yes); COSERO can only transfer water from a source basin to one single receiving basin	-

[a] Derived for basin delineation B.

Appendix B

Table B1: Overview of the river regions.

No.	Name of river region	Area [km²] [a]	Important headwaters and tributaries
1	Rhine	7 610	Anterior Rhine, Posterior Rhine, Plessur, Landquart, Ill, Frutz
2	Danube above Inn	49 942	Iller, Brenz, Wörnitz, Lech, Altmühl, Naab, Regen, Isar, Ilz, Vils
3	Inn above Salzach	15 249	Sanna, Ötztaler Ache, Sill, Ziller, Brandenberger Ache, Brixentaler Ache, Mangfall, Alz
4	Salzach	6 684	Krimmler Ache, Fuscher Ache, Gasteiner Ache, Großarlbach, Lammer, Saalach
5	Inn under Salzach	4 060	Mattig, Mühlheimer Ache, Rott, Pram
6	Danube between Inn and Traun	2 870	Erlau, Große Mühl, Innbach
7	Traun	3 851	Ischl, Ager, Krems
8	Danube between Traun and Enns	342	Gusen
9	Enns	5 997	Salza, Steyr
10	Danube between Enns and Morava	15 492	Aist, Naarn, Ybbs, Erlauf, Melk, Pielach, Kamp, Schwechat, Fischa
11	Vltava	763	Maltsch
12	Morava	25 688	Bečva, Thaya
13	Danube between Morava and Leitha	1 073	-
14	Leitha [b]	2 118	Schwarza
15	Rabnitz [b]	777	Einser-Kanal
16	Raab [b]	4 416	Lafnitz, Pinka
17	Mur [b]	9 908	Taurach, Pöls, Liesing, Mürz, Kainach, Sulm
18	Drava [b]	12 000	Isel, Möll, Lieser, Gail, Gurk, Lavant

[a] Area which is covered by basin delineation B. [b] River joins the Danube outside the project area in Hungary / Croatia.

1130 **Appendix C**

Table C1: Calibrated parameters in the hydrological model COSERO.

Parameter	Description	Default value	Lower constraint	Upper constraint	Unit

BETA	Parameter to compute runoff generation as a function of soil moisture	4.5	0.1	10	-
CTMAX	Maximum snow melt factor on June 21	2	1 (5 [b])	7	mm °C^{-1} d^{-1}
CTMIN	Minimum snow melt factor on Dec 21	5	1	7	mm °C^{-1} d^{-1}
QDIV_RATIO [c]	Ratio of the water amount which is transferred to the receiving basin and the water amount which flows to the intake in the source basin	0.5	0	0.9	-
ETSLPCOR	Factor to correct PET	1	0.5	2	-
FKFAK	Factor to compute ETA from PET as a function of soil moisture	0.7	0.1	1	-
H1	Outlet level of reservoir for simulating surface flow	2	1	20	mm
H2	Outlet level of reservoir for simulating interflow	10	0	50	mm
KBF	Recession constant for simulating outflow from the soil module with a linear reservoir	3 000	1 000	10 000	h
M	Storage capacity of the soil	[a]	10	500	mm
NVAR	Variance for distributing new snowfall with a log-normal distribution	1.5	0	10 (5 [b])	-
RAINTRT	Transition temperature above which precipitation is pure rain	3	0	4	°C
SNOWTRT	Transition temperature below which precipitation is pure snow	0.5	-2	2	°C
TAB1	Recession constant for simulating surface flow	50	1	200	h
TAB2	Recession constant for simulating interflow	250	1	500	h
TAB3	Recession constant for simulating baseflow	5 000	10	10 000	h
TAB4	Recession constant for simulating routing	1	0.05	10	h
TAB5	Additional time shift for simulating routing	1	0.05	20	h
TVS1	Recession constant for simulating percolation from the surface flow module	100	1	400	h
TVS2	Constant for simulating percolation from the inter flow module	500	1	1 000	h

[a] parameter "soil_tawc" (Table A8). [b] for basins with a mean catchment elevation ("elev_mean" in Table A3) of at least 2 000 m a.s.l. [c] calibrated only if there is a cross-basin water transfer (see file "Crossbasin_water_transfers.csv", Table A11), otherwise parameter is set to 0.

Table C2: Provided input / output time series from the hydrological model COSERO.

Variable	Description	Unit	References
YYYY	Year	-	-
MM	Month	-	-
DD	Day	-	-
P_	Precipitation sum [a]	mm	ERA5L (Muñoz Sabater, 2019a)
T_	Mean air temperature [a]	°C	ERA5L (Muñoz Sabater, 2019a)
PET_	Sum of potential evapotranspiration (PET) following Thornthwaite [a]	mm	Thornthwaite and Mather (1957)
ETA_	Sum of actual (total) evapotranspiration (ETA) [a]	mm	-
BW0_	Water level of soil storage [a]	mm	-
BW3_	Water level of groundwater storage [a]	mm	-
SWW_	Snow water equivalent [a]	mm	-
Qsim_	Simulated runoff [a,b]	$m^3\ s^{-1}$	-
Qobs_	Observed runoff [a]	$m^3\ s^{-1}$	BAFU (2020), CHMI (2020), GKD (2020), HZB (2020), LUBW (2020)

[a] Suffix "_A" indicates that aggregation was done for basin delineation A (full upstream topographic catchment area), while suffix "_B" indicates aggregation for basin delineation B (intermediate catchments). [b] Set to "-999", if basin was calibrated together with the next downstream basin due to less runoff observations in calibration period.